REPORT DOCUMENTATION PAGE		Form Approved OMB No. 0704-0188

1a. REPORT SECURITY CLASSIFICATION UNCLASSIFIED	1b. RESTRICTIVE MARKINGS
2a. SECURITY CLASSIFICATION AUTHORITY	3. DISTRIBUTION/AVAILABILITY OF REPORT
2b. DECLASSIFICATION/DOWNGRADING SCHEDULE	Approved for public release; distribution is unlimited.

4. PERFORMING ORGANIZATION REPORT NUMBER(S) ARL-TR-89-4	5. MONITORING ORGANIZATION REPORT NUMBER(S)

6a. NAME OF PERFORMING ORGANIZATION Applied Research Laboratories	6b. OFFICE SYMBOL (if applicable) ARL:UT	7a. NAME OF MONITORING ORGANIZATION Office of the Chief of Naval Research
6c. ADDRESS (City, State, and ZIP Code) The University of Texas at Austin P.O. Box 8029 Austin, Texas 78713-8029		7b. ADDRESS (City, State, and ZIP Code) Department of the Navy Arlington, Virginia 22217-5000
8a. NAME OF FUNDING/SPONSOR ORGANIZATION	8b. OFFICE SYMBOL (if applicable)	9. PROCUREMENT INSTRUMENT IDENTIFICATION NUMBER N00014-87-K-0392

8c. ADDRESS (City, State, and ZIP Code)	10. SOURCE OF FUNDING NUMBERS			
	PROGRAM ELEMENT No.	PROJECT No.	TASK No.	WORK UNIT ACCESSION No.

11. TITLE (Include Security Classification) Experimental Study of Remote Sensing of Particle Motion by Crosscorrelation of Acoustic Backscatter

12. PERSONAL AUTHOR(S) Chotiros, Nicholas P.

13a. TYPE OF REPORT final	13b. TIME COVERED 87-6-1 TO 88-9-30	14. DATE OF REPORT (Year, Month, Day) 89-2-7	15. PAGE COUNT 85

16. SUPPLEMENTARY NOTATION

17. COSATI CODES			18. SUPPLEMENTARY NOTATION
FIELD	GROUP	SUB-GROUP	sonar; remote sensing, correlation, flow measurement

19. ABSTRACT (Continue on reverse if necessary and identify by block number)

There are particles suspended in the ocean, such as bubbles and biological debris, which can backscatter acoustic waves. In a previous design study, it was determined that the backscatter from a collection of particles could produce a detectable and unique acoustic signature. Since the particles are often passive riders, it would be feasible to track the movement of the water by using a sonar and a crosscorrelation method. The acoustic signature of scatterers and the operation of an acoustic tracker were simulated on a computer. A signal simulator generates a set of backscattered signals for a multibeam sonar system. The scatterers are pinged as their positions are changed in a way that simulates flows and eddies in the water. Crosscorrelating signals from successive pings, a reasonably accurate portrayal of the water motion was demonstrated for irrotational motion. A small experimental sonar was constructed and tested in a laboratory tank and in the field. In the tank, the sonar was used to track a moving wall and a bubble stream. In the field, the sonar was used to track naturally occurring bubbles.

20. DISTRIBUTION/AVAILABILITY OF ABSTRACT ☐ UNCLASSIFIED/UNLIMITED ☒ SAME AS RPT. ☐ DTIC USERS	21. ABSTRACT SECURITY CLASSIFICATION UNCLASSIFIED
22a. NAME OF RESPONSIBLE INDIVIDUAL John M. Huckabay	22b. TELEPHONE (Include Area Code) 512-835-3588	22c. OFFICE SYMBOL ASG

DD form 1473, JUN 86   Previous editions are obsolete.

TABLE OF CONTENTS

LIST OF FIGURES

v

LIST OF TABLES

ACKNOWLEDGMENTS

1. INTRODUCTION

This project has been an experimental study of the concept of acoustic remote sensing of ocean surface and volume movements. It may lead to the development of acoustic remote sensing systems that will provide the capability to observe the movement of the ocean surface and volume for a wide variety of experimental applications, such as the observation of the interaction between wind, waves, and the water mass, and the study of currents, eddies, and internal wave motion both in the open ocean and under ice caps.

The two main problems in such a study are detection and motion estimation. A design study[1] was completed in 1986 in which it was found that, using naturally occurring scatterers that are passive riders such as bubbles and plankton, it should be possible to obtain detectable acoustic echoes from the water volume and thus track water volume movements. The water surface, under rough surface conditions, is a strong acoustic scatterer that can be detected acoustically without much difficulty. The motion of surface and bottom scatterers is illustrated in Fig. 1.1. Thus, the acoustic detection of surface and volume scatterers was judged to be quite feasible.

The next problem is the determination of the three-dimensional motion of the ocean surface and volume from the acoustic backscattered signal. Detection and measurement of the velocity component in the radial direction by Doppler and correlation methods have been successfully demonstrated in several related applications.[2-5] The measurement of motion in the remaining two principal directions, however, has only been demonstrated in a few instances[6-9] and requires further research.

Our approach is to initially divide the field of view into resolvable cells, and then track the three-dimensional motion of the cloud of scatterers from each cell, by the range and angle displacement of its acoustic backscatter signature, as illustrated in Fig. 1.2. In the next section, the immediate objectives are formally described. To minimize costs, the experimental demonstration was limited to the remote sensing of two-dimensional motion. In Section 3, the computer simulation model used to generate test signals is described. In Section 4, the signal

1
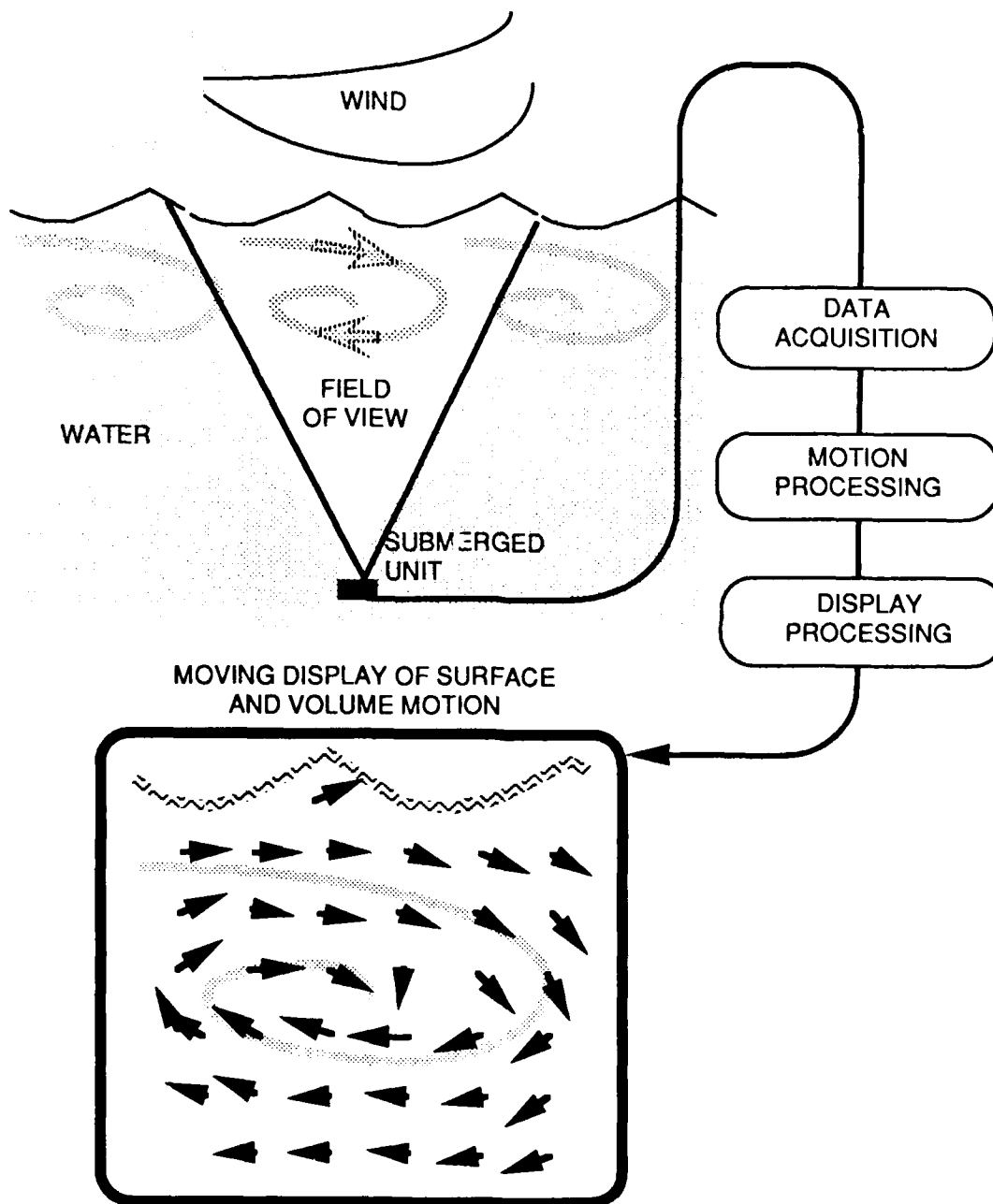
FIGURE 1.1
REMOTE SENSING SONAR CONCEPT
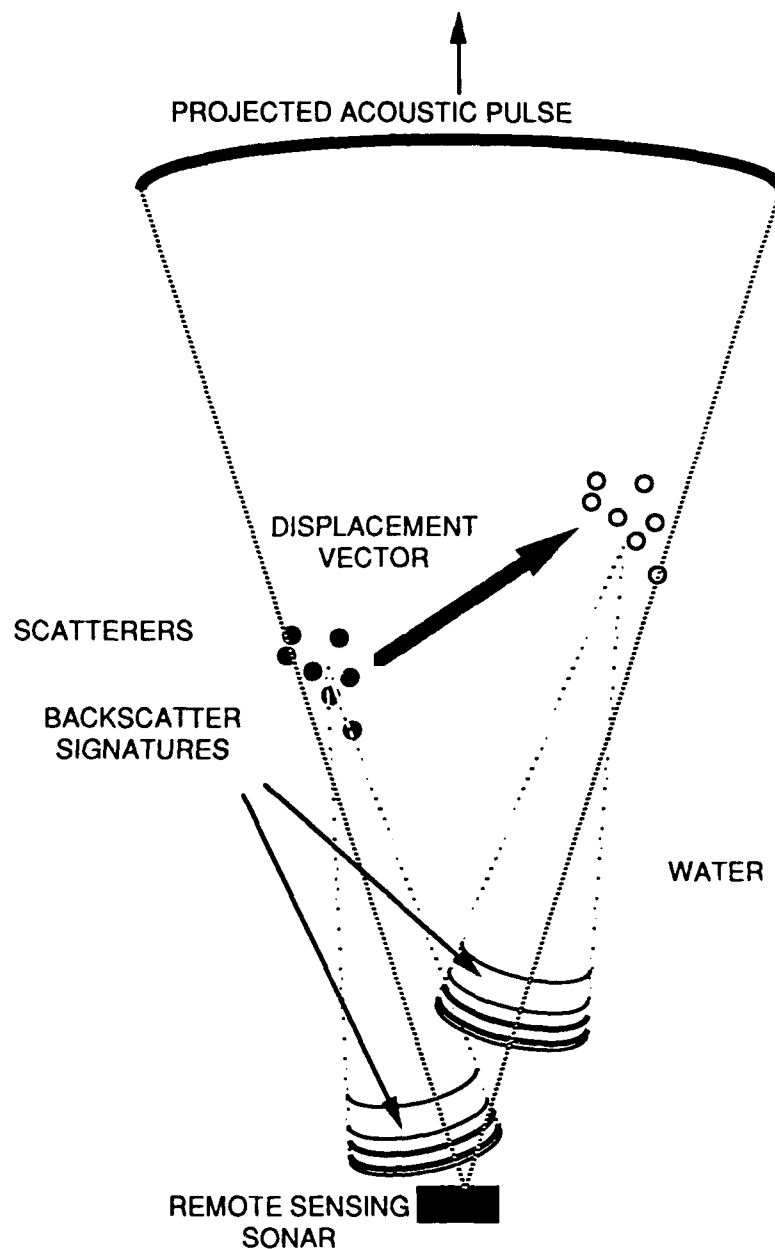
FIGURE 1.2
TRACKING SCATTERERS BY THEIR ACOUSTIC
SIGNATURES

3

processing and motion estimation algorithms are formulated. Three motion processing algorithms were developed, each differing in the degree of wavefront coherence assumed. In Section 5, the results obtained using the three motion processing algorithms with the computer simulated data are described. In Section 6, these results are analyzed. It was found that the third method, which assumed no wavefront coherence, had the best performance for translational motion. For rotational motion, however, all three methods performed poorly. In Section 7, the laboratory and field experiments and their results are described. Finally, in Section 8, conclusions are drawn and plans for future work are put forward, including possible approaches to combining translational and rotational motion, and the computer simulation of full scale three-dimensional remote sensing systems.

2. OBJECTIVES

The objective is to experimentally demonstrate the feasibility of particle motion tracking by crosscorrelation of the acoustic backscatter, in a multidimensional space including time delay, range, and angle. In order to minimize costs, it was decided to limit the demonstration to two-dimensional motion only, which meant that a line array could be used instead of a planar array. The plan called for the construction of a small acoustic line array to observe and record the acoustic backscatter produced by a variety of water surface and volume movements within a field of view defined by a 3° by 12° projector beam. The field of view was divided into a number of resolution cells of approximately 0.15 m by 0.15 m (6 in. by 6 in.). Experiments were performed both in a laboratory tank and in the field. The data were then processed by computer to produce estimates of two-dimensional particle motion. Agreement between the experimental results and ground truth would constitute a demonstration of feasibility.

3. COMPUTER SIMULATION OF ACOUSTIC BACKSCATTER

In order to allow algorithm development to progress in parallel with hardware development, a computer program was written to simulate the acoustic backscatter from volume scatterers to provide test data for development and controlled testing of the signal processing software.

The simulation model generates a set of Q point scatterers within an initial volume that encompasses the field of view. A general point scatterer q is initially given a random position $z_{q,0}$ and a random complex scattering cross section $\sigma(q)$. Between successive pings, the position is changed by a transformation operator T. Thus, its position $z_{q,k}$ at the kth ping is given by $z_{q,0}T^k$. Several types of transformation operators were written, including linear translation, rotation, and continuous and discontinuous shear deformation. The number of scatterers used are typically between 5000 and 20,000. The sonar is modeled with one projector and a hydrophone array, all at rest. The scatterers are assumed to be in the farfield of the projector and the hydrophone array elements. The signal pulse is modeled as a carrier tone at frequency ω_0 modulated by an arbitrary pulse $p(t)$. Although $p(t)$ may be arbitrarily chosen, a cw pulse is normally used. The backscattered acoustic signal $s(t,i,k)$ at time t, from the ith receiver and on the kth ping, is constructed by superposition, assuming single scatter only, giving

$$s(t,i,k) = \sum_{q=1}^{Q} \frac{\sigma(q)\, p(t-\tau_{q,i,k})\, D_p (z_{q,k} - z_p)\, D_i (z_{q,k} - z_i)}{|z_{q,k} - z_p|\, |z_{q,k} - z_i|}\, e^{j\omega_0 (t-\tau_{q,i,k})} \quad , \tag{3.1}$$

where z_i and z_p are the positions of the hydrophone and projector, respectively, $D_i (.....)$ and $D_p (.....)$ are their directivity functions, and $\tau_{q,i,k}$ is the two-way propagation delay between the scatterer and the sonar. The geometry is illustrated in Fig. 3.1. For simplicity, the directivity functions are assumed to be frequency independent within the operating frequency band of the system.

Finally, the signals $s(t,i,k)$ from the array of M_i hydrophones are sampled at a sampling interval τ_0, giving a sampled data series $s(n_t\tau_0,i,k)$ containing N samples per ping for each hydrophone. The sampling interval is chosen to satisfy the
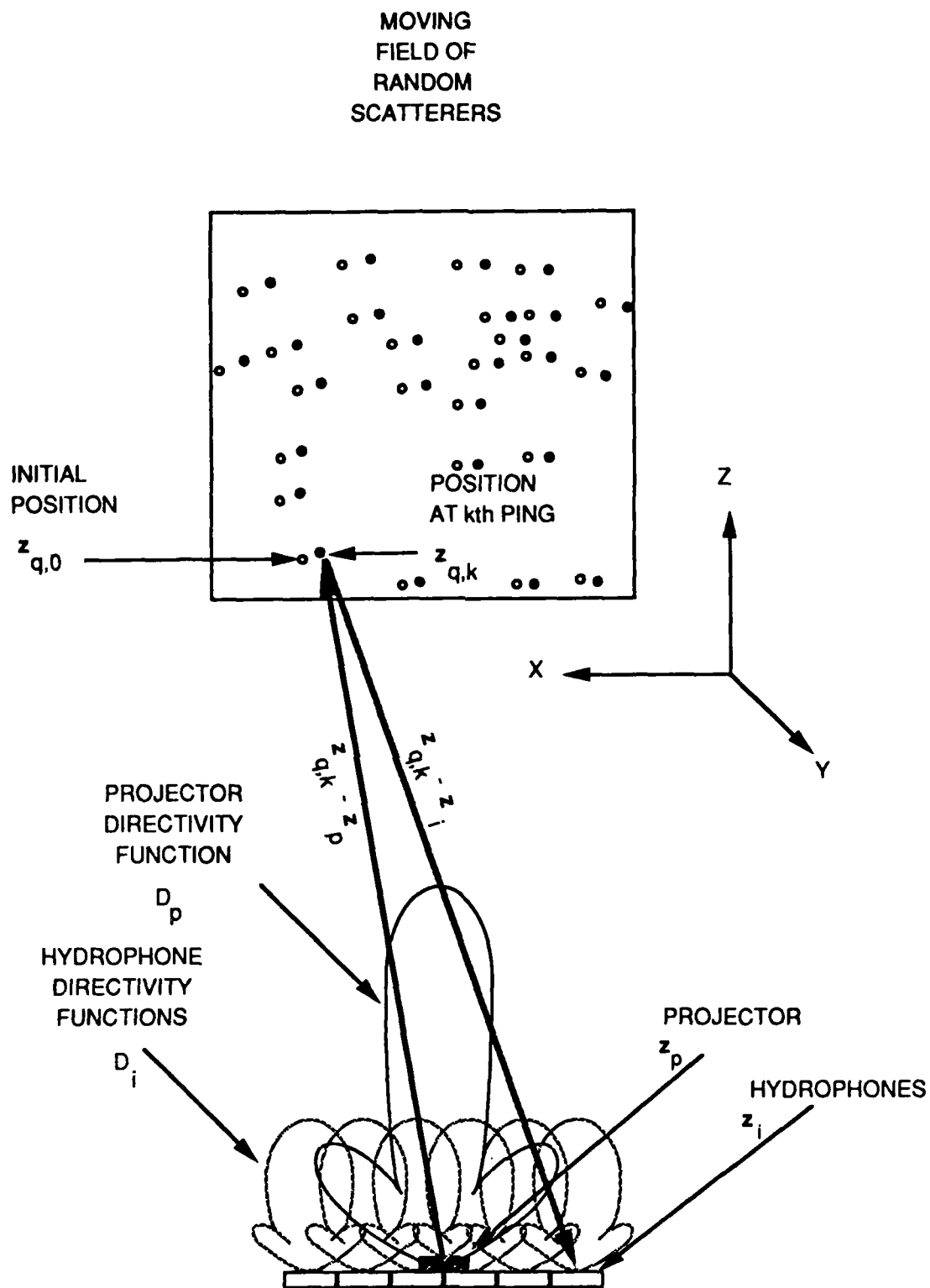
FIGURE 3.1
COMPUTER SIMULATION GEOMETRY

Nyquist conditions. The data series is then passed to the signal processing block. Data from a real sonar array are also presented in the same format to allow the results from real and simulated data to be directly compared.

4. SIGNAL PROCESSING

The field of view is considered to be segmented, by angle and range in a polar coordinate system, into a number of arbitrary and overlapping cells. Algorithms are required to process the acoustic backscatter from each cell and ping and produce estimates of the water movement between adjacent cells as a function of time. The signal, as received at the hydrophone array, must first be preprocessed to give the acoustic backscatter signature from each cell. Then, the motion estimation algorithm may be applied to obtain estimates of the particle movements. Three methods or algorithms are described, referred to as Methods A, B, and C. These methods differ in the degree of wavefront coherence that the backscatter signature may be assumed to possess. Finally, the results are displayed. Many types of displays are possible and it is not clear if there is a best one for all situations. We have chosen to use a moving velocity vector map because it allows the performance of the motion estimation algorithms to be checked directly. The processing scheme is shown in Fig. 4.1.

4.1 PREPROCESS

Before processing, the signals are beamformed and grouped into subsets according to a predetermined system of resolution cells. Let the field of view be divided into an arbitrary number of cells by beam and slant range. Let the slant range be divided into N_r overlapping intervals, n_a samples apart, each interval containing a block of n_b samples. The number of samples n_b should be large enough to allow a sufficient time-bandwidth product for a recognizable acoustic signature in accordance with the analysis contained in the design study.[1] Each cell is uniquely addressed by its ping number k, beam number m, and range interval number r. The signal samples b(n,r,m,k) from each cell are addressed by the sample number n, where n has a value between 1 and n_b.

The signal samples in each cell are obtained by grouping the signal samples from the hydrophone array into corresponding blocks in range and then beamforming each block to give an arbitrary number of beams M. The angular coordinates θ(m) of the mth beam will, in a three-dimensional remote sensing problem, include both the azimuth and elevation angles; in this study, by limiting

11
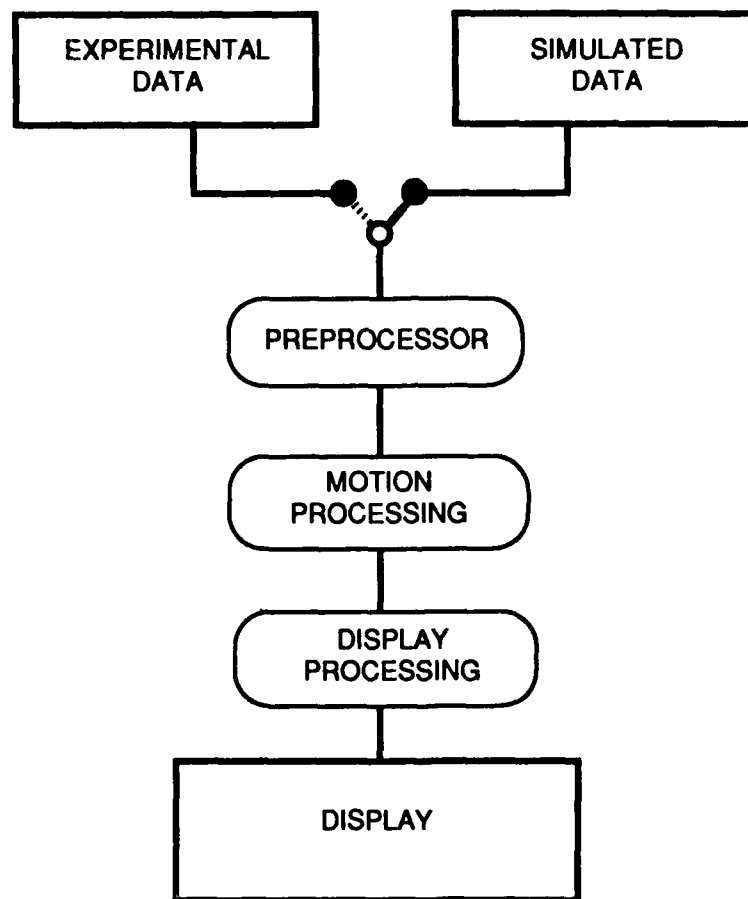
**FIGURE 4.1
DATA PROCESSING
SCHEME**

ourselves to a two-dimensional problem, $\theta(m)$ is simply the azimuth angle. Thus, the nth signal sample from the rth range interval, mth beam, and kth ping $b(n,r,m,k)$ is given by

$$b(n,r,m,k) = \sum_{i=1}^{M_i} s(n_t \tau_0 - \tau_{i,r,m},i,k); \quad n_t = (r-1)n_a+1, \ldots (r-1)n_a+n_b \quad , \qquad (4.1)$$

where $\tau_{i,r,m}$ is the time delay of the rth range interval from the ith element for the mth beam. Time delaying is accomplished by applying linear phase shifts to the Fourier transform of the input samples $s(n_t \tau_0, i, k)$ from each range interval. Beamforming each range interval separately allows stepwise focusing for improved nearfield performance. The series of complex signal samples $s(n_t \tau_0, i, k)$ could come either directly from the simulator or from a real hydrophone array via a Hilbert transform.

The signal set $B(r,m,k)$, from a cell in the kth ping, mth beam, and rth range interval is defined as

$$B(r,m,k) = \{b(1,r,m,k), b(2,r,m,k), \ldots b(n_b,r,m,k)\} \quad . \qquad (4.2)$$

Our approach is to estimate motion from the movement of the crosscorrelation function of the signals $B(r,m,k)$ through a multidimensional space of time delay (ping), range, and angle. Three different algorithms were developed based on this approach. The first, which will be called Method A, is the direct approach in which the backscattered signatures from each beam/range cell of a ping are crosscorrelated with those of another ping. Coherent wavefronts are implicitly assumed.

The second and third algorithms, called Methods B and C, were designed for partially coherent wavefronts. They require several sets of beams with spatially separated acoustic centers. Each set of beams is formed from a subarray of M_J elements out of the total array of M_i elements. The coordinates of the acoustic center $v(j)$ of the jth subarray is a point on the array. In a three-dimensional remote sensing problem, $v(j)$ would be a two-dimensional coordinate on a planar array. In

13

this study, it is a point on a line array. The beamed signal samples $b(n,r,m,j,k)$ from the jth subarray are given by

$$b(n,r,m,j,k) = \sum_{i=j}^{j+M_j-1} s(n_t \tau_0 - \tau_{i,r,m,j}, i,k); \quad n_t = (r-1)n_a+1, \ldots (r-1)n_a+n_b \quad , \quad (4.3)$$

where $\tau_{i,r,m,j}$ are the time delays of the jth subarray.

For Methods B and C, the signal set $B(r,m,j,k)$, from a cell in the kth ping, jth subarray, mth beam, and rth range interval, is defined as

$$B(r,m,j,k) = \{b(1,r,m,j,k), b(2,r,m,j,k), \ldots b(n_b,r,m,j,k)\} \quad . \quad (4.4)$$

4.2 MOTION ESTIMATION ALGORITHMS

The three methods or algorithms referred to as Methods A, B, and C will now be described. These methods differ in the degree of wavefront coherence that may be assumed. Method A assumes complete coherence, while Methods B and C assume limited coherence and no coherence, respectively.

4.2.1. Method A: Crosscorrelation and Beam Interpolation

In this method, we use the direct approach of searching for crosscorrelation peaks to determine the movement of scatterers between cells. Let us assume that the acoustic backscatter signature from the cloud of scatterers within a cell, as detected by the whole hydrophone array in a ping k_1, is unique and recognizable at a later ping k_2. It is implicitly assumed that the backscatter signature is coherent over the whole hydrophone array, as illustrated in Fig. 4.2.

The signals are organized in sets according to Eq. (4.2). The crosscorrelation function $C(n_\tau, r_1, r_2, m_1, m_2, k_1, k_2)$, as a function of the sample difference n_τ between a cell at range r_1, beam m_1, from ping k_1, and a cell at beam m_2, range r_2, from ping k_2 is computed as a sum of crossproducts thus,

14

FIGURE 4.2
METHOD A: TEMPORAL SIGNATURE RECOGNITION AND RADIAL
DISPLACEMENT ESTIMATION BY PING-PING CROSSCORRELATION,
AND ANGULAR DISPLACEMENT ESTIMATION BY BEAM INTERPOLATION

15

$$C(n_\tau, r_1, r_2, m_1, m_2, k_1, k_2)$$

$$= B(r_2\text{-}n/n_b, m_2, k_2) \bullet B^*(r_1, m_1, k_1)$$

$$= \sum_{n=0}^{n_b-1} b(r_2 n_a + n + n_\tau, m_2, k_2) \, b^*(r_1 n_a + n, m_1, k_1) \quad , \qquad (4.5)$$

where * denotes complex conjugation.

For a given reference cell (r_1, m_1) in ping k_1, the search space (n_τ, r_2, m_2) in ping k_2 is searched for the largest magnitude of the crosscorrelation function. Let the crosscorrelation function have a peak at a point ($n_{\tau p}, r_{2p}, m_{2p}$) in the search space. Let the movement of the water particles initially in the cell (r_1, m_1), from ping k_1 to ping k_2, be modeled in terms of radial ρ_d and angular θ_d displacements, as illustrated in Fig. 4.2. The radial component of displacement ρ_d is given by

$$\rho_d = (n_{\tau p} + (r_{2p} - r_1) \, n_a) \, \tau_o c_o / 2 \quad , \qquad (4.6)$$

where c_o is the speed of sound in water.

The angular displacement θ_d is simply given by the difference between the angular coordinates,

$$\theta_d = \theta(m_{2p}) - \theta(m_1) \quad . \qquad (4.7)$$

In practice, the angular difference between preformed beams may be too coarse. Either an interpolation or a monopulse process may be used to improve the angular sensitivity. Both processes are likely to have comparable performance. Only the interpolation process will be described. Thus,

$$\theta_d = \theta_{2p} - \theta(m_1) \quad , \qquad (4.8)$$

where θ_{2p} is the estimated direction of the scatterer cloud in ping k_2. As an interpolation problem, θ_{2p} may be formulated as a weighted mean of the angular coordinates of the beams adjacent to m_{2p}.

16

$$\theta_{2p} = \frac{\Sigma_\kappa \, \theta(\kappa) \, a_\kappa}{\Sigma_\kappa \, a_\kappa} \quad , \tag{4.9}$$

where a_κ is a weighting function, and Σ_κ denotes a summation over all values of the beam number κ representing beams in the vicinity of m_{2p}. From a probabilistic approach, the weighting function is an estimate of the likelihood of a particular angle. Therefore, it should be equated to the square of the magnitude of the associated crosscorrelation function,

$$a_\kappa = \left| C(n_{\tau p}, \, r_1, \, r_{2p}, \, m_1, \, \kappa, \, k_1, \, k_2) \right|^2 \quad . \tag{4.10}$$

4.2.2 Method B: Beam Interpolation with Multi-Subarrays

In Method A, it is implicitly assumed that the backscatter signature is coherent over the whole hydrophone array. In practice, this may not be the case. Therefore, in Method B, the backscatter signature is taken from only a subset of the hydrophones in the array, implicitly assuming that the signal is coherent over the subarray, as illustrated in Fig. 4.3. Any azimuthal movement or rotation of the scatterer cloud will produce changes in both the arrival angle and the position on the hydrophone array of the signature.

The input signals are organized according to Eq. (4.4). The cross-correlation function $C(n_\tau, r_1, r_2, j_1, j_2, m_1, m_2, k_1, k_2)$, as a function of the lag in sample periods nt, between a cell at range r_1, subarray j_1, beam m_1, from ping k_1, and a cell at range r_2, subarray j_2, beam m_2, from ping k_2 is computed as a sum of cross products thus,
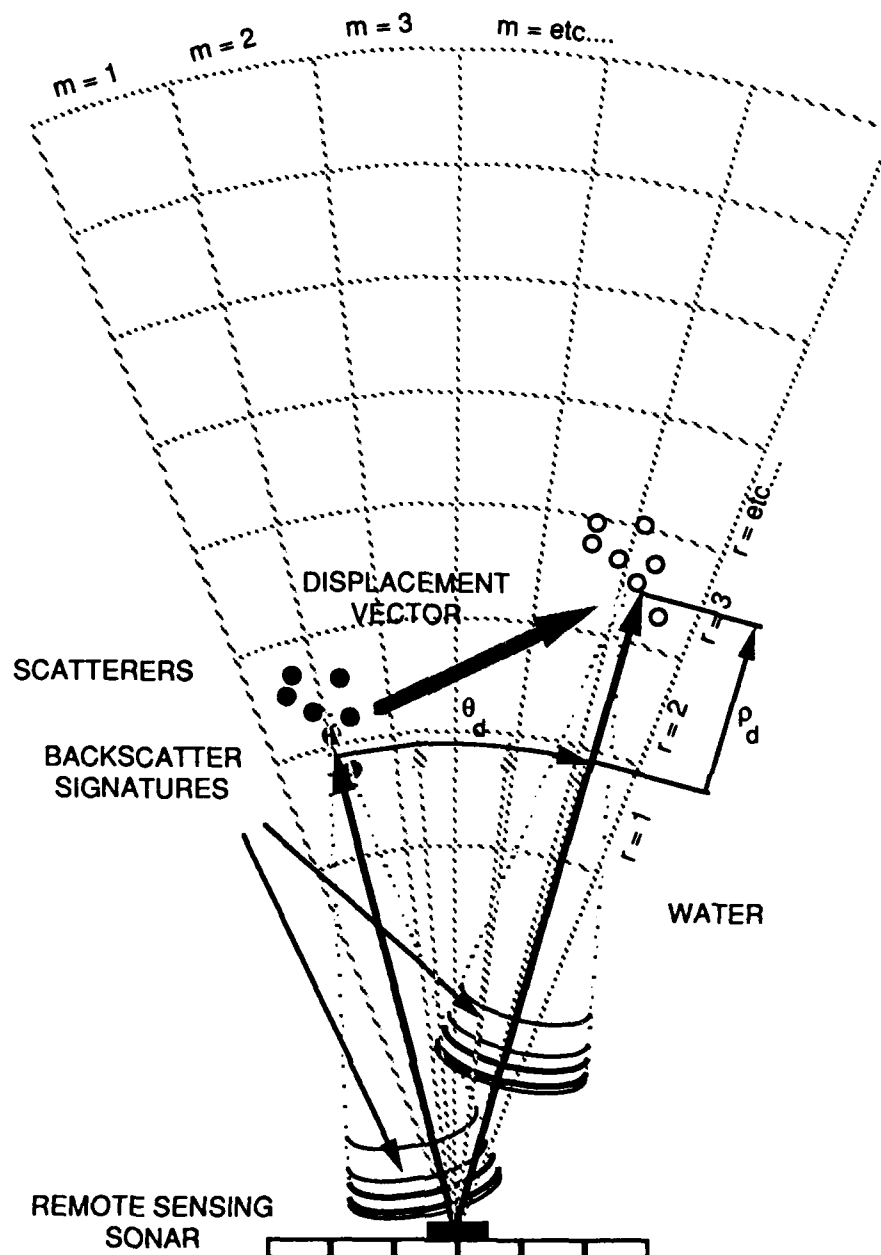
FIGURE 4.3
**METHOD B: TEMPORAL SIGNATURE RECOGNITION AND RADIAL
DISPLACEMENT ESTIMATION BY PING-PING CROSSCORRELATION,
LATERAL AND ANGULAR DISPLACEMENT ESTIMATION BY
INTERPOLATION**

$$C(n_\tau, r_1, r_2, j_1, j_2, m_1, m_2, k_1, k_2)$$

$$= B(r_2\text{-}n/n_b, m_2, j_2, k_2) \bullet B^*(r_1, m_1, j_1, k_1)$$

$$= \sum_{n=0}^{n_b-1} b(r_2 n_a + n + n_\tau, m_2, j_2, k_2)\, b^*(r_1 n_a + n, m_1, j_1, k_1) \quad . \qquad (4.11)$$

For a given reference cell (r_1, m_1) of subarray j_1 in ping k_1, the search space (n_τ, r_2, m_2, j_2) in ping k_2 is searched for the largest magnitude of the crosscorrelation function. Let the crosscorrelation function have a peak at a point ($n_{\tau p}, r_{2p}, m_{2p}, j_{2p}$).

The movement of the cloud of scatterers initially in the cell (r_1, m_1), from ping k_1 to ping k_2, is modeled in terms of radial and angular displacements, as in Method A, plus a lateral component, shown in Fig. 4.4. The angular θ_d and lateral λ_d displacements of the acoustic signature are the result of azimuthal translation x_d and rotation θ_r. Applying geometrical ray theory and assuming small angles, the displacement tensor (x_d, z_d, θ_r) is obtained in terms of the measurables ($\theta_d, \lambda_d, \rho_d$). Thus, this method not only gives an estimate of the translational components of motion (x_d, z_d), but also a rotational component θ_r.

The radial and angular displacements are estimated according to Eqs. (4.6) through (4.10) as under Method A, except that a subarray is used instead of the whole array.

The lateral displacement of the acoustic signature along the array λ_d is given by

$$\lambda_d = v(j_2) - v(j_1) \quad . \qquad (4.12)$$

An interpolation algorithm may also be used to improve the sensitivity of the λ_d estimator, in a similar way to that of the angular displacement component. Thus, following the same steps as in Eqs. (4.7) through (4.10),
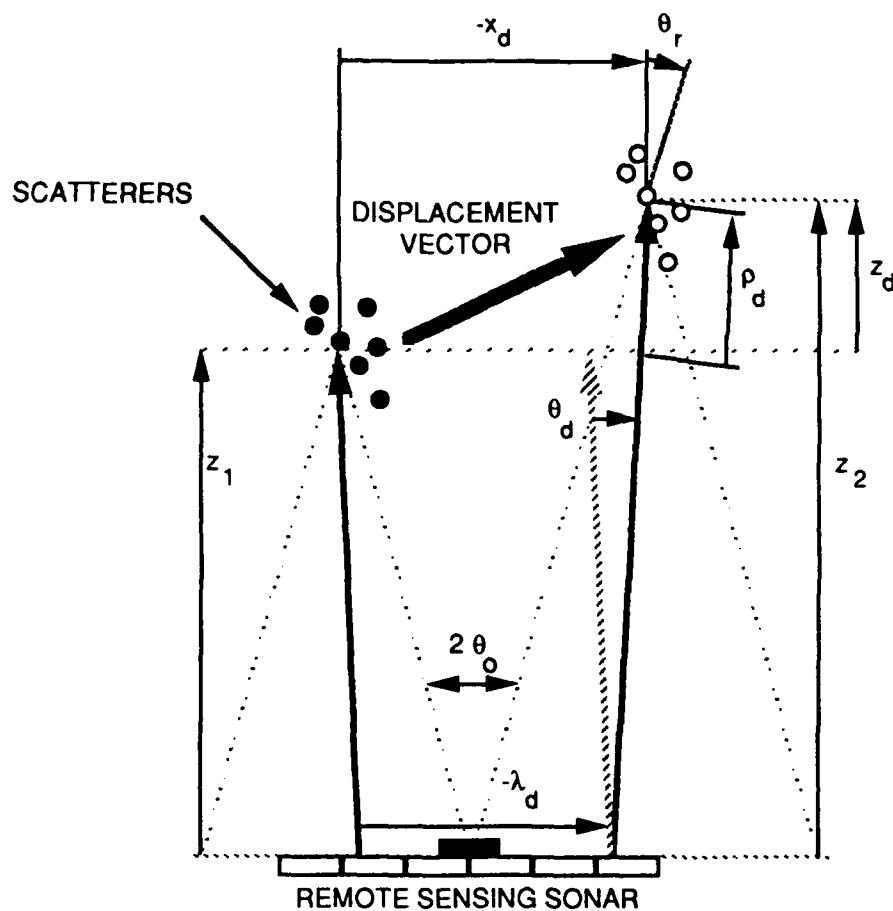
MOTION TENSOR IN TERMS
OF THE MEASURABLES
ASSUMING SMALL ANGLES

$$z_d = \rho_d$$

$$\theta_r = \theta_d - \lambda_d / (2z_1 + \rho_d)$$

$$x_d = \lambda_d - \theta_d (z_1 + \rho_d /2)$$

FIGURE 4.4
PARTICLE CLOUD MOVEMENT MODELED IN TERMS OF RANGE,
LATERAL AND ANGULAR DISPLACEMENT COMPONENTS

$$\lambda_d = v_{j2} - v(j_1) \quad , \tag{4.13}$$

where

$$v_{j2} = \frac{\Sigma_\kappa \, v(\kappa) \, b_\kappa}{\Sigma_\kappa \, b_\kappa} \tag{4.14}$$

and

$$b_\kappa = \left| C(n_{xp}, \, r_1, \, r_{2p}, \, m_1, \, m_{2p}, \, j_1, \, \kappa, \, k_1, \, k_2) \right|^2 \quad . \tag{4.15}$$

4.2.3 Method C: Zero Rotation Assumption

In Method B, the backscatter signature is assumed to be coherent over the hydrophone subarray used for beamforming. In the event that even this limited degree of spatial coherence is absent, then any form of processing that relies on a coherent wavefront, such as direction finding by beam interpolation, would be inapplicable. Without the beam interpolation, the remaining components of Method B could still be used if the rotation of the scatterer cloud is known. Where the flow is mainly translational, and free of shear or rotational motion, it is possible to apply the remainder of Method B. This variation will be referred to as Method C.

The movement of the cloud of scatterers initially in a cell (r_1, m_1), from ping k_1 to ping k_2, is modeled in terms of lateral, radial, and angular displacements, but assuming zero rotation, as shown in Fig. 4.5. It can be seen that the azimuthal displacement is approximately half the lateral displacement.

4.2.4 Discrimination of Discrete and Distributed Scatterers

The multi-subarray approach in Methods B and C can distinguish between the backscatter from discrete scatterers and a cloud of scatterers. A discrete scatterer, in this case, is defined as a dominant but compact scatterer such that the hydrophone is in its farfield. The discrete scatterer produces a backscatter
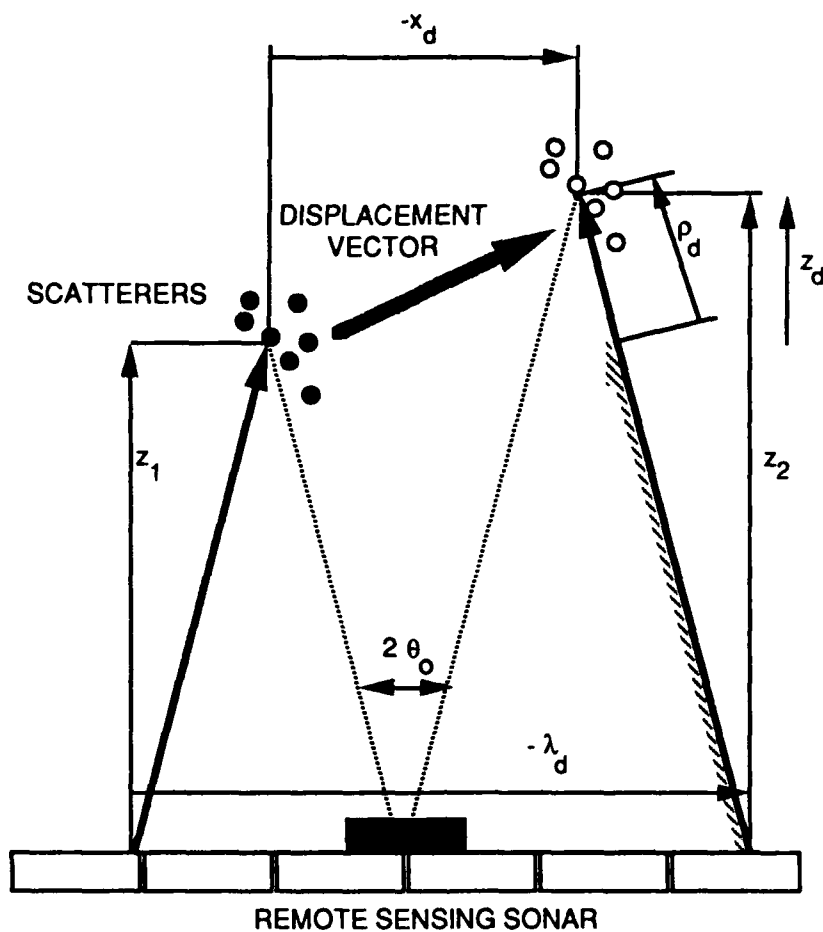
MOTION TENSOR IN TERMS
OF THE MEASURABLES
ASSUMING SMALL ANGLES

$$z_d = \rho_d$$

$$x_d = \lambda_d / 2$$
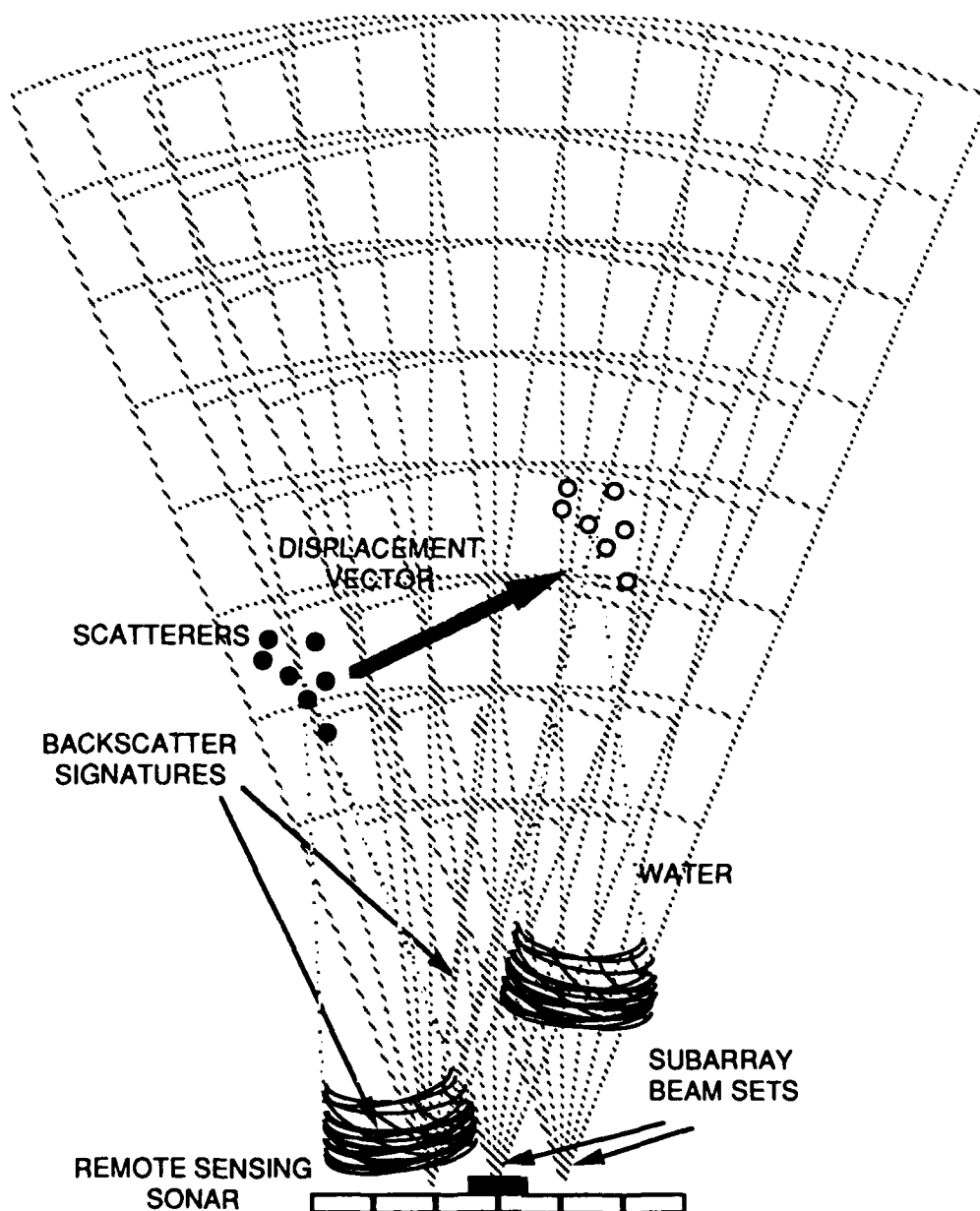
FIGURE 4.5
METHOD C: TEMPORAL SIGNATURE RECOGNITION AND RADIAL
DISPLACEMENT ESTIMATION BY PING-PING CROSSCORRELATION,
LATERAL DISPLACEMENT ESTIMATION BY INTERPOLATION ASSUMING
ZERO ROTATION OF THE SCATTERER CLOUD

with a coherent wavefront and produces identical signals at all subarrays. The cloud of distributed scatterers, as will be demonstrated in Section 6.2, does not produce coherent wavefronts and therefore the backscatter at each subarray is uncorrelated. Thus, unlike the distributed cloud of scatterers, the discrete scatterer may be distinguished by the property that the crosscorrelation function of its backscatter does not have a maximum in the jth dimension of the search space. This property may be used to distinguish discrete scatterers, such as individual fish and other unwanted objects, from the volume backscatter of the passive riders, such as bubbles and plankton.

4.3 SURFACE MOTION

A smooth surface is impossible to map from one point since the only returns would be the specular reflections. In order to successfully map the surface profile, it is necessary to have a sufficient degree of roughness to reduce the specular reflections and generate detectable backscatter over a large range of grazing angles. Therefore, a minimum sea state number is required for successful surface mapping. Given that a sufficient degree of roughness is present, the above algorithms should be able to determine the motion of both volume and surface elements. In practice, with surfaces and interfaces one is often more interested in the profile than the velocity. A simple acoustic profiler would be more appropriate. Therefore, a profiler was also programmed into the processing software which simply detected signal peaks and plotted their positions according to their propagation delay and beamed direction.

5. COMPUTER SIMULATION RESULTS

The simulations were made for a geometry that closely matched that of the experimental sonar system for the purposes of making comparisons with the experimental results at a later stage. A Cartesian coordinate system is adopted in which the sonar is at the origin and the broadside direction coincides with the z axis. Thus, the sonar was modeled as a single projector and a hydrophone line array of six elements, with physical dimensions identical to those of the experimental sonar. The line array is coincident with the x axis. The dimensions are shown in Fig. 5.1. Since only a line array is used, the system was limited to sensing two-dimensional motion coplanar with the line array, that is, in the x-z plane. The field of view is centered at a point approximately 6 m in front of the sonar, coordinates (0,0,6). In each case, all three methods were tried. The simulated ping repetition rate was set at one ping per second for convenience.

Computer simulated signals were generated for a number of representative types of volume motion to be used as test cases, including linear translation, rotation, and shear. The simulations are listed in Table 5.1.

The results obtained are described below. In each case, a diagram illustrating the scatterer motion is shown. A second diagram compares the ideal result with the results obtained by the three methods in the form of a motion tensor display.

The motion of the scatterers is illustrated in Fig. 5.2. The results obtained by the three methods are compared with the ideal result in Fig. 5.3. The ideal result is labeled by the letter "I". The results obtained by the three methods are labeled A, B, and C, accordingly. The translational displacement over a specified period of the scatterer cloud in each cell is represented by an arrow. In this case, it should point in the z direction, which is straight up. The length of the arrow indicates the magnitude of the velocity according to the velocity scale provided.

25

FIELD OF VIEW

HYDROPHONE
ARRAY
ELEMENTS

Z

X

0.061 m

0.0203 m

Y

0.14 m

0.050 m

PROJECTOR

0.018 m
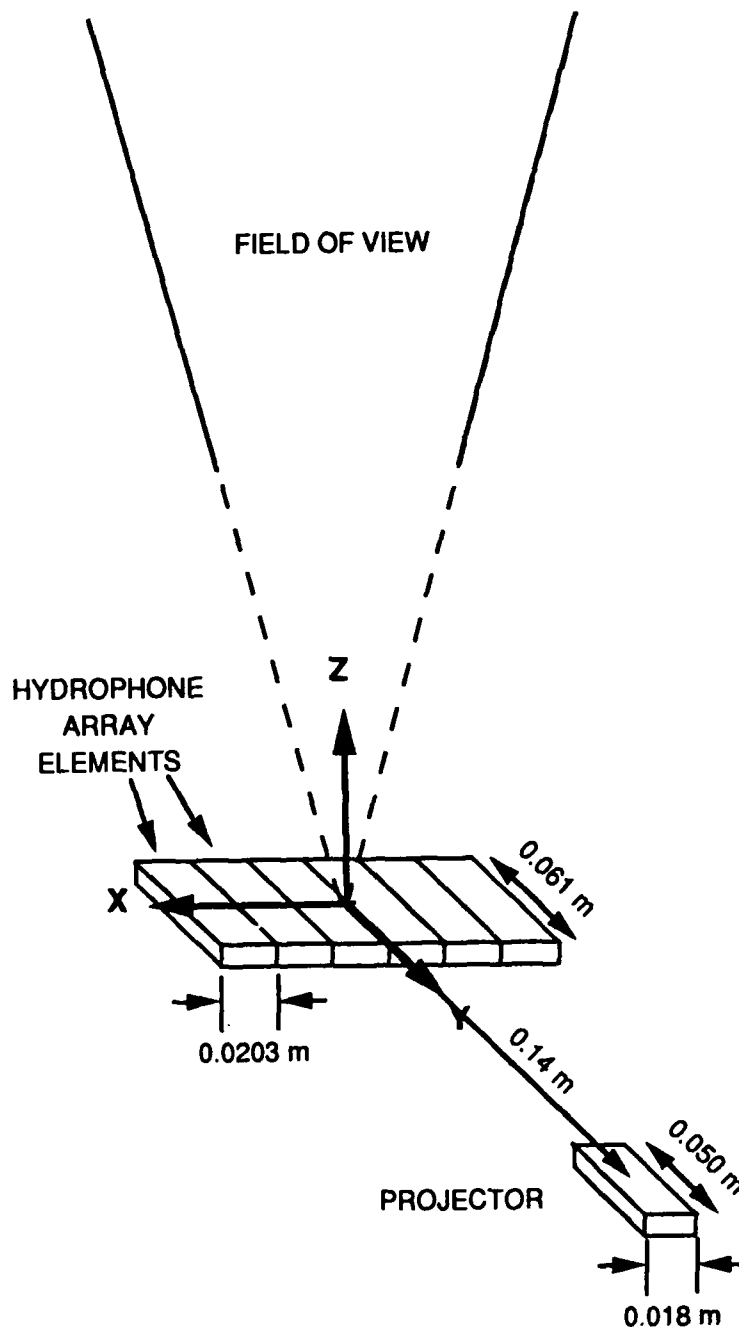
FIGURE 5.1
DIMENSIONS OF THE ACOUSTIC ARRAY IN THE COMPUTER
SIMULATIONS

TABLE 5.1

COMPUTER SIMULATED TEST CASES OF VOLUME MOTION

Case	Description
1	Translational motion in the axial direction, at an initial velocity of 3 cm/s and accelerating at 1 cm/s^2.
2	Translational motion in the azimuthal (cross-range) direction, at an initial velocity of 3 cm/s and accelerating at 1 cm/s^2.
3	Constant velocity regions separated by a planar shear boundary at an angle of 6° relative to the z direction in the x-z plane, with velocities 3 cm/s parallel to the boundary.
4	Constant velocity regions separated by a planar sink boundary, at an angle of 17° relative to the z direction in the x-z plane, with velocities 1 cm/s towards the boundary.
5	Constant rate of shear in the azimuth (cross-range) direction of 0.01 rad/s about the plane at z=5.3.
6	Rotation at an initial angular velocity of 0.003 rad/s and accelerating at 0.0001 rad/s^2, about a point initially at the center of the field of view (0,0,6) and moving at a velocity of (0.1,0,1) cm/s.
7	Constant rate of shear in the axial direction of 0.003 rad/s about the y-z plane.
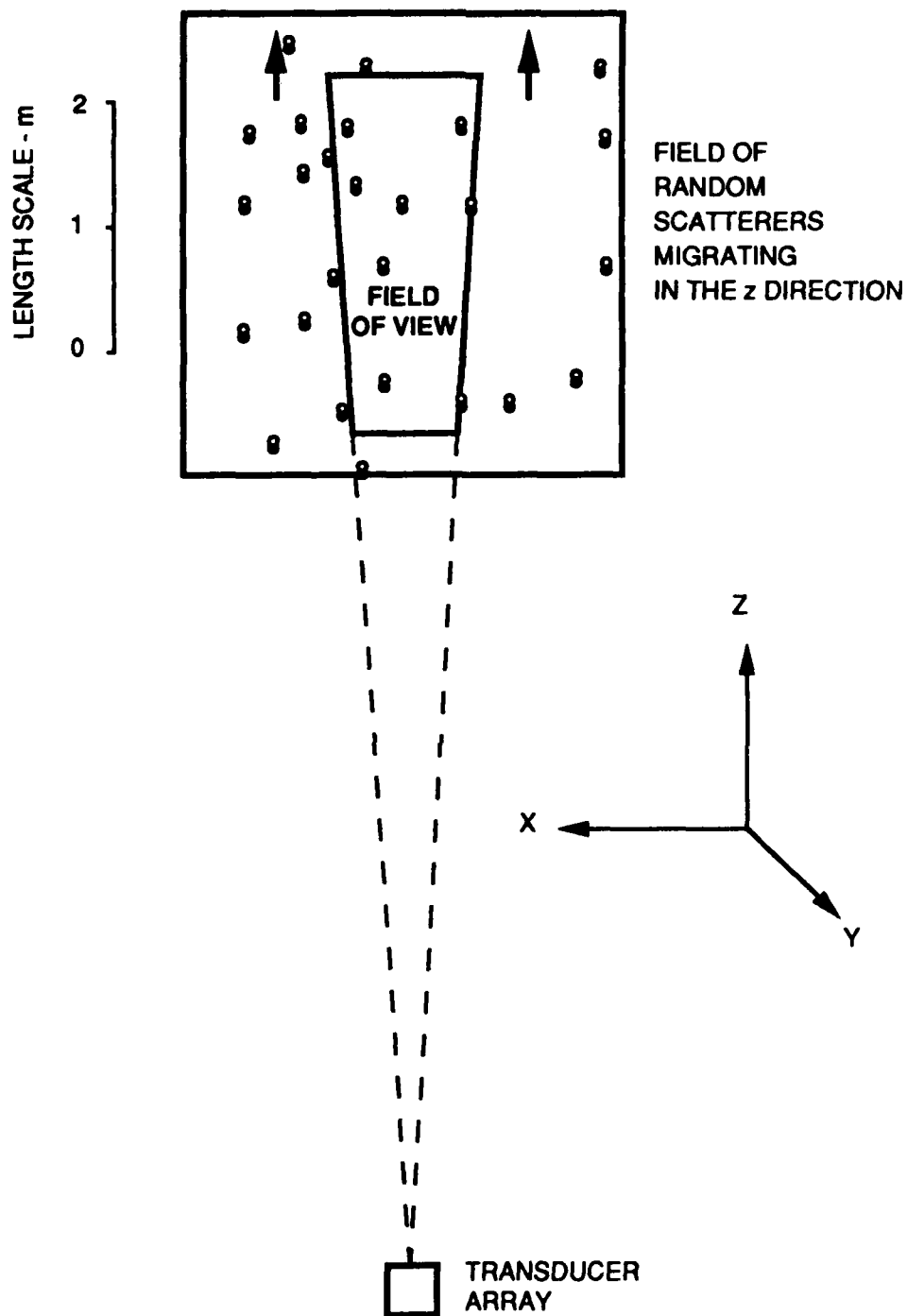
FIGURE 5.2
REMOTE SENSING SIMULATION OF A RANDOM SCATTERER FIELD MOVING IN THE z DIRECTION

I - IDEAL VELOCITY VECTORS
A - FULL ARRAY + BEAM INTERPOLATION
B - SUBARRAYS + BEAM INTERPOLATION
C - SUBARRAYS + ZERO ROTATION
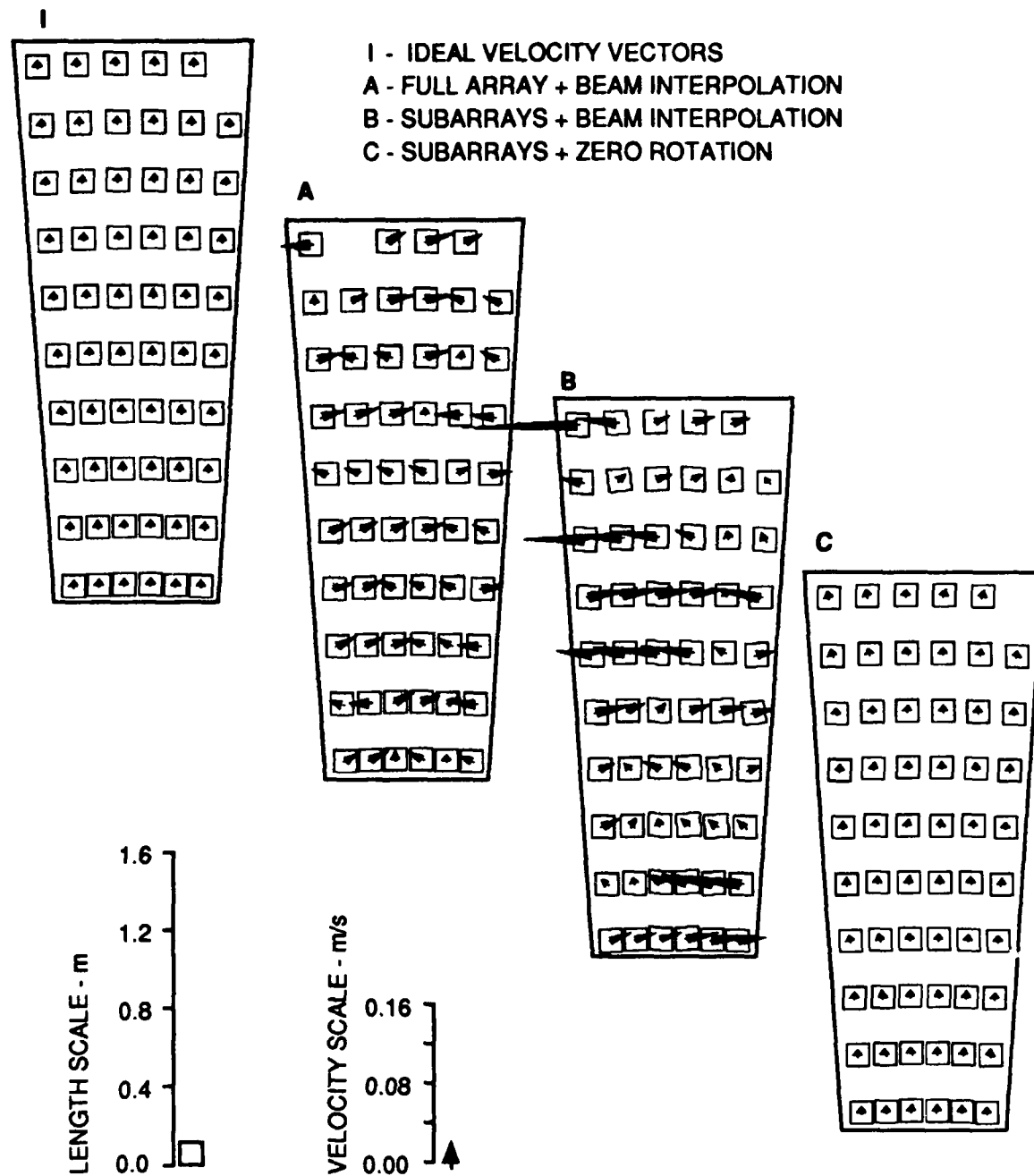
FIGURE 5.3
GRAPHICAL COMPARISON OF METHODS FOR A RANDOM SCATTERER
FIELD MOVING IN THE z DIRECTION

29

5.1 CASE 1: TRANSLATIONAL MOTION IN THE AXIAL DIRECTION

The distance between cells may be measured using the length scale provided. The rotation of the box frame around each arrow vector represents the rotational component of the displacement tensor; this is only applicable to the ideal tensor and Method B. Method A is not able to give rotation estimates and Method C assumes that the rotation is zero. A small amount of acceleration was also included in the simulation to test for sensitivity to acceleration.

It is seen in Fig. 5.3 that Methods A and B gave erroneous results. Method C gave results that agree very well with the ideal reference.

5.2 CASE 2: TRANSLATIONAL MOTION IN THE AZIMUTHAL DIRECTION

The motion of the scatterers is illustrated in Fig. 5.4. The results obtained by the three methods are compared with the ideal result in Fig. 5.5. Again, it is seen that Methods A and B were unable to correctly estimate the velocity. Method C was able to estimate the velocity, although not without noticeable random errors in the velocity magnitude.

5.3 CASE 3: PLANAR SHEAR BOUNDARY BETWEEN CONSTANT VELOCITY REGIONS

The motion of the scatterers is illustrated in Fig. 5.6. The results obtained by the three methods are compared with the ideal result in Fig. 5.7. It was found that Method A was unable to obtain the minimum correlation peaks for processing. It is seen that Method B produced results with gross errors in angular displacement. Method C, however, appears to be able to track the flow velocities on both sides of the shear boundary.

FIGURE 5.4
REMOTE SENSING SIMULATION OF A RANDOM SCATTERER FIELD
MOVING IN THE x DIRECTION

I - IDEAL VELOCITY VECTORS
A - FULL ARRAY + BEAM INTERPOLATION
B - SUBARRAYS + BEAM INTERPOLATION
C - SUBARRAYS + ZERO ROTATION
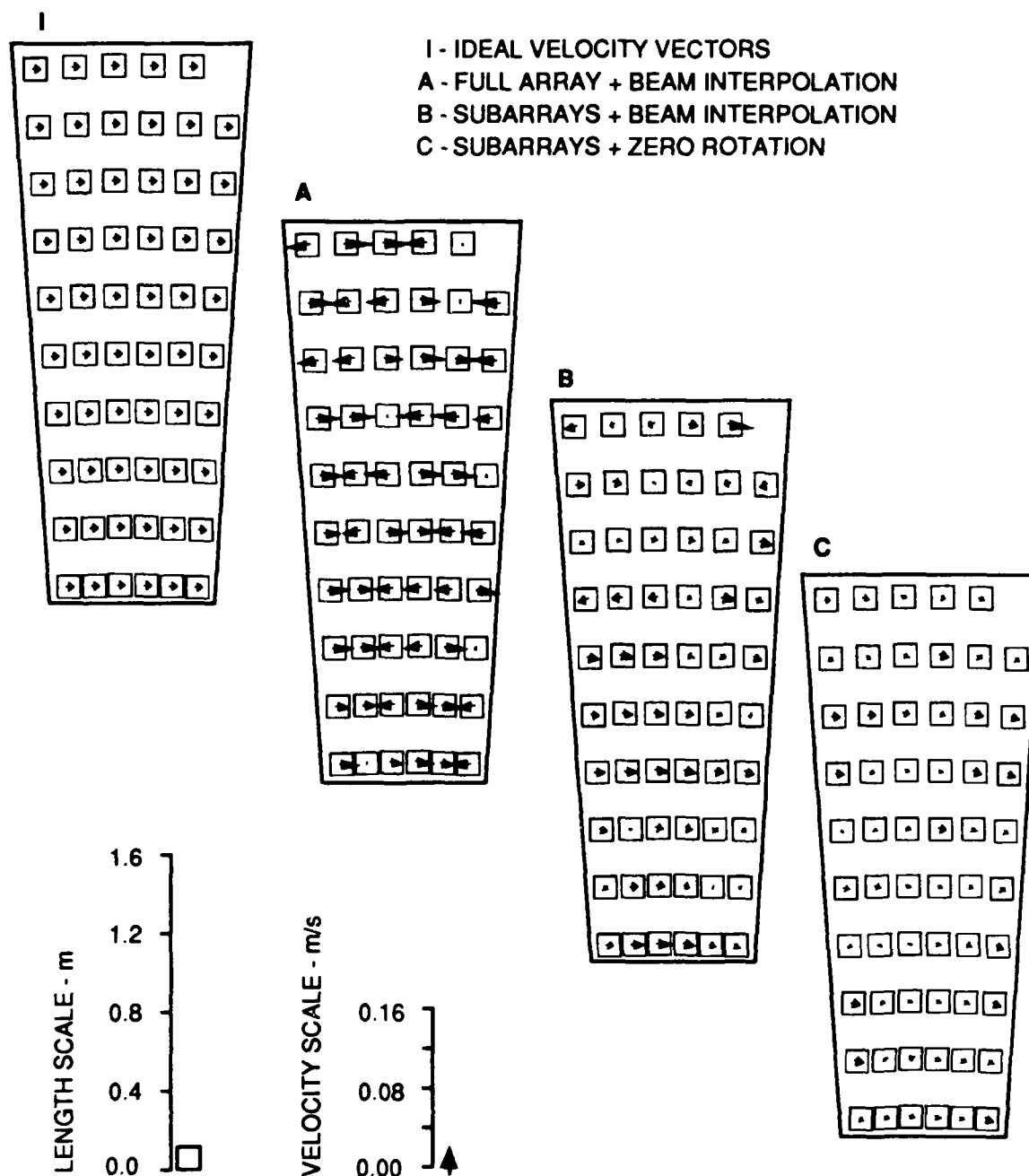
FIGURE 5.5
GRAPHICAL COMPARISON OF METHODS FOR A RANDOM SCATTERER
FIELD MOVING IN THE x DIRECTION

LENGTH SCALE - m

FIELD
OF VIEW

FIELD OF
RANDOM
SCATTERERS
WITH SHEAR BOUNDARY

Z

X

Y

TRANSDUCER
ARRAY

FIGURE 5.6
REMOTE SENSING SIMULATION OF A RANDOM SCATTERER FIELD
OF CONSTANT VELOCITY REGIONS
SEPARATED BY A PLANAR SHEAR BOUNDARY

I - IDEAL VELOCITY VECTORS
A - FULL ARRAY + BEAM INTERPOLATION
B - SUBARRAYS + BEAM INTERPOLATION
C - SUBARRAYS + ZERO ROTATION

FIGURE 5.7
GRAPHICAL COMPARISON OF METHODS FOR A RANDOM SCATTERER FIELD
OF CONSTANT VELOCITY REGIONS
SEPARATED BY A PLANAR SHEAR BOUNDARY

34

5.4 CASE 4: PLANAR SINK BETWEEN CONSTANT VELOCITY REGIONS

The motion of the scatterers is illustrated in Fig. 5.8. The results obtained by the three methods are compared with the ideal result in Fig. 5.9. It was found that Method A was unable to obtain the minimum correlation peaks for processing. It is seen that Method B produced results with gross errors in angular displacement. Method C, however, appears to be able to 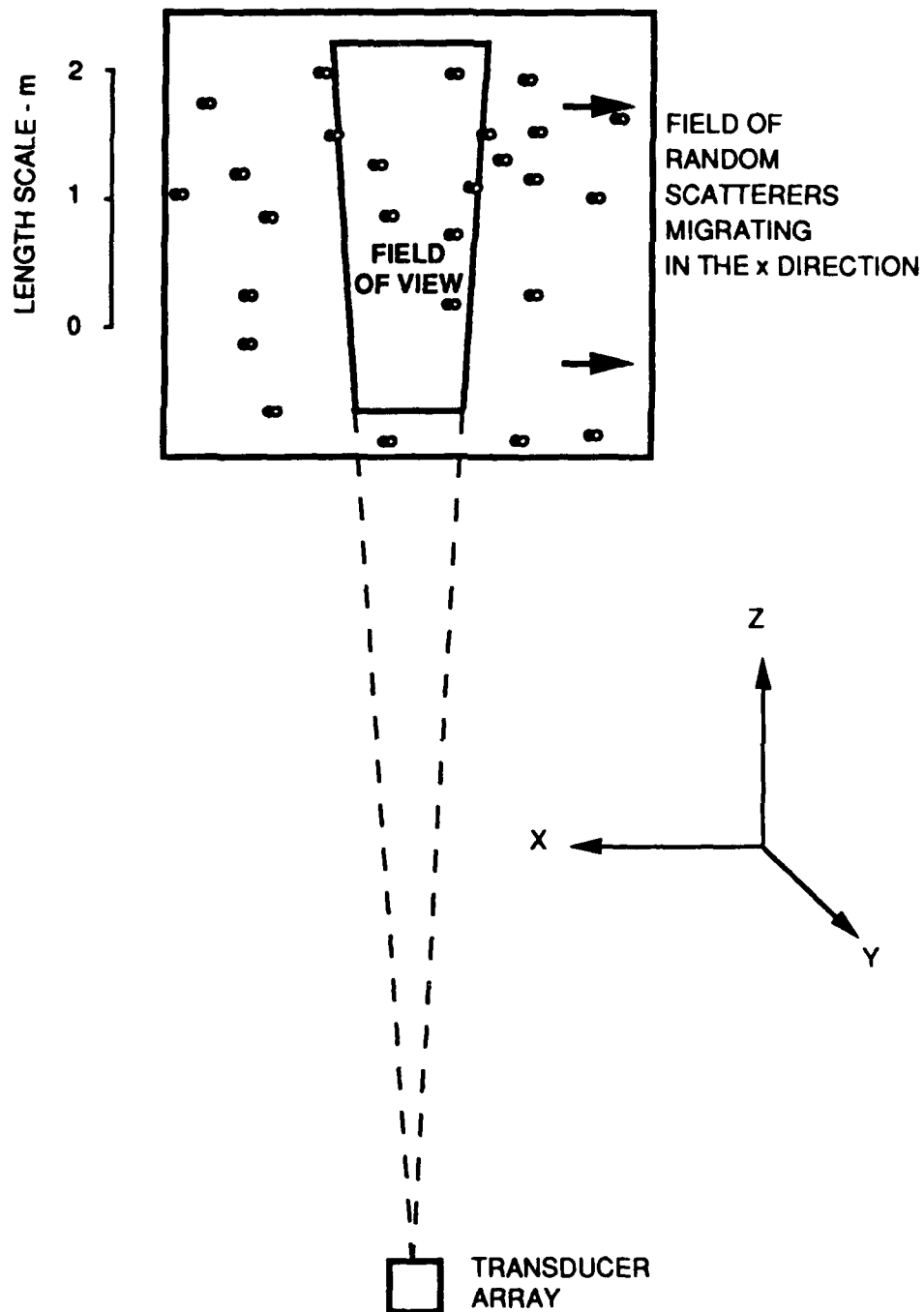track the flow velocities on both sides of the sink boundary, with the exception of a few errors in the immediate vicinity of the boundary.

5.5 CASE 5: CONSTANT RATE OF SHEAR IN THE AZIMUTH DIRECTION

The motion of the scatterers is illustrated in Fig. 5.10. The results obtained by the three methods are compared with the ideal result in Fig. 5.11. It was found that Method A was unable to obtain the minimum correlation peaks for processing. It is seen that Method B produced results with gross errors in angular displacement. Method C, however, appears to be able to track the flow velocities, although not without noticeable random errors in the velocity magnitude.

5.6 CASE 6: CONSTANT ROTATION ABOUT THE CENTER OF THE FIELD OF VIEW

The motion of the scatterers is illustrated in Fig. 5.12. The results obtained by the three methods are compared with the ideal result in Fig. 5.13. It is seen that Methods A and B produced results with gross errors in angular displacement. Method C produced results with a gross consistent error caused by the zero rotation assumption. This is because the algorithm in Method C cannot distinguish between rotational effects and azimuthal translation. Thus, a clockwise rotation is interpreted as an azimuthal movement from right to left as shown in the results.

At the stated ping repetition rate, a higher rate of shear caused the correlation peaks to be lost entirely, due to the deflection of the signature pattern from one ping, to a point completely outside the hydrophone array, on the next ping.
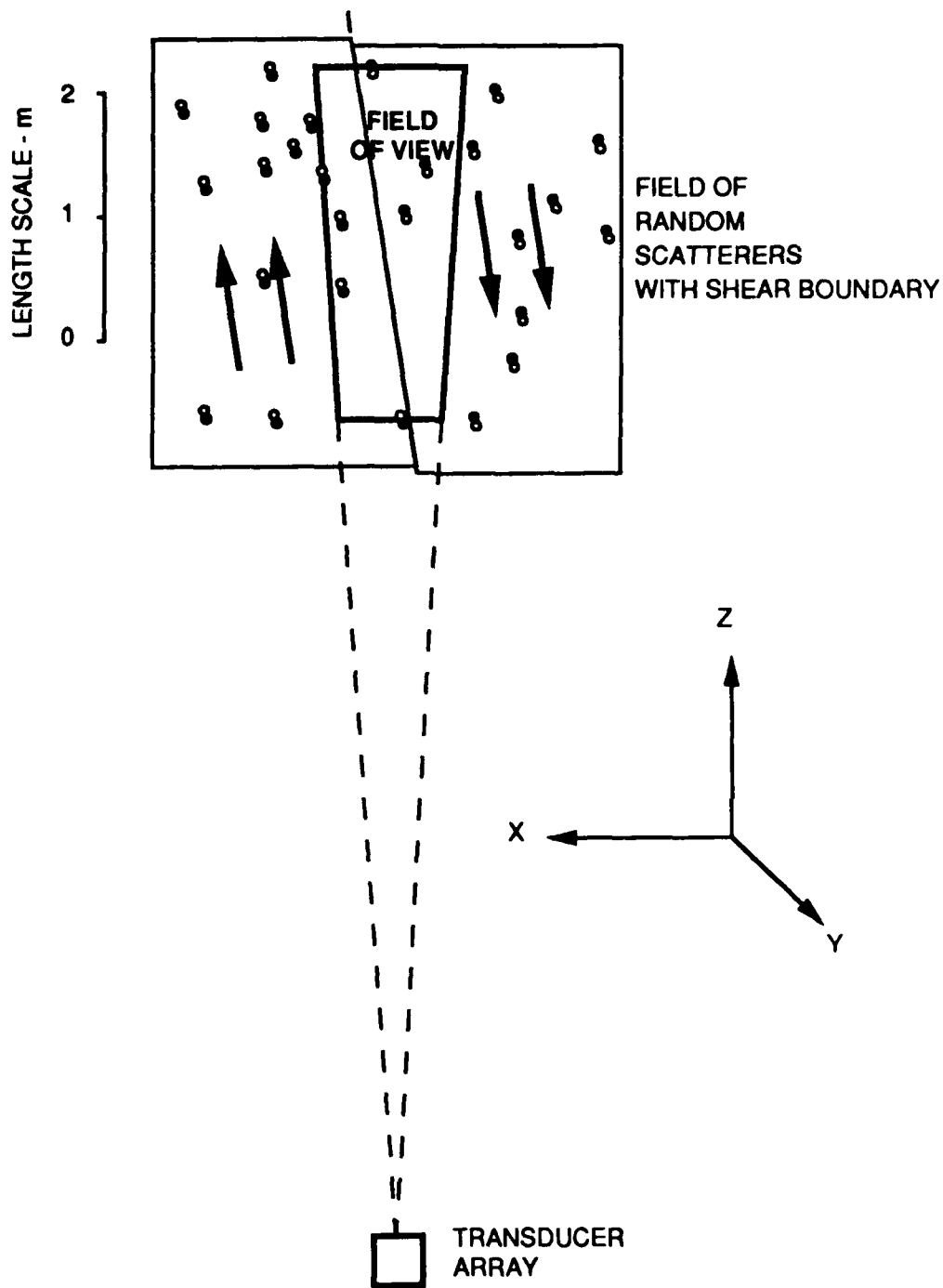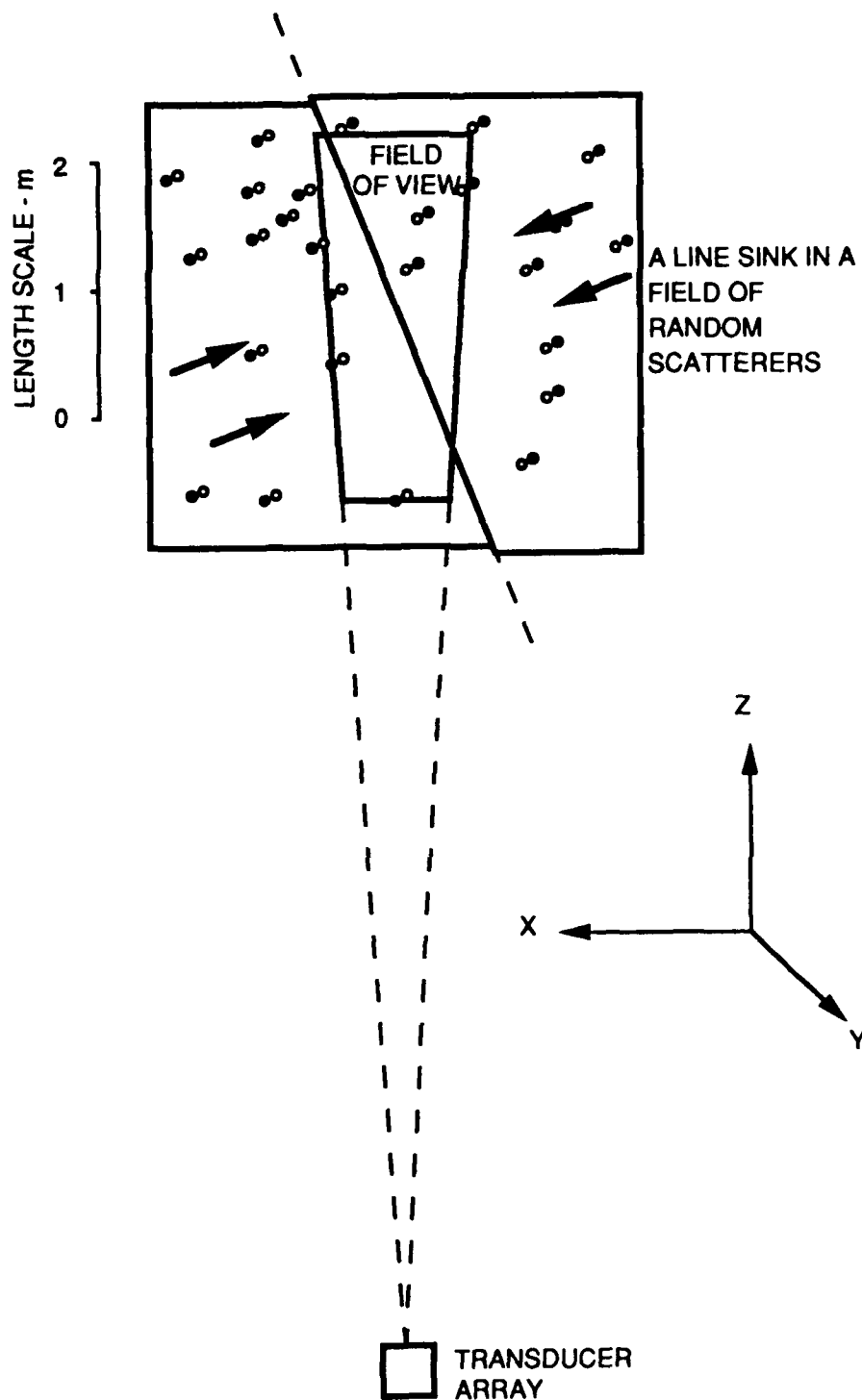
FIGURE 5.8
REMOTE SENSING SIMULATION OF A RANDOM SCATTERER FIELD
OF CONSTANT VELOCITY REGIONS
SEPARATED BY A PLANAR SINK BOUNDARY

I - IDEAL VELOCITY VECTORS
A - FULL ARRAY + BEAM INTERPOLATION
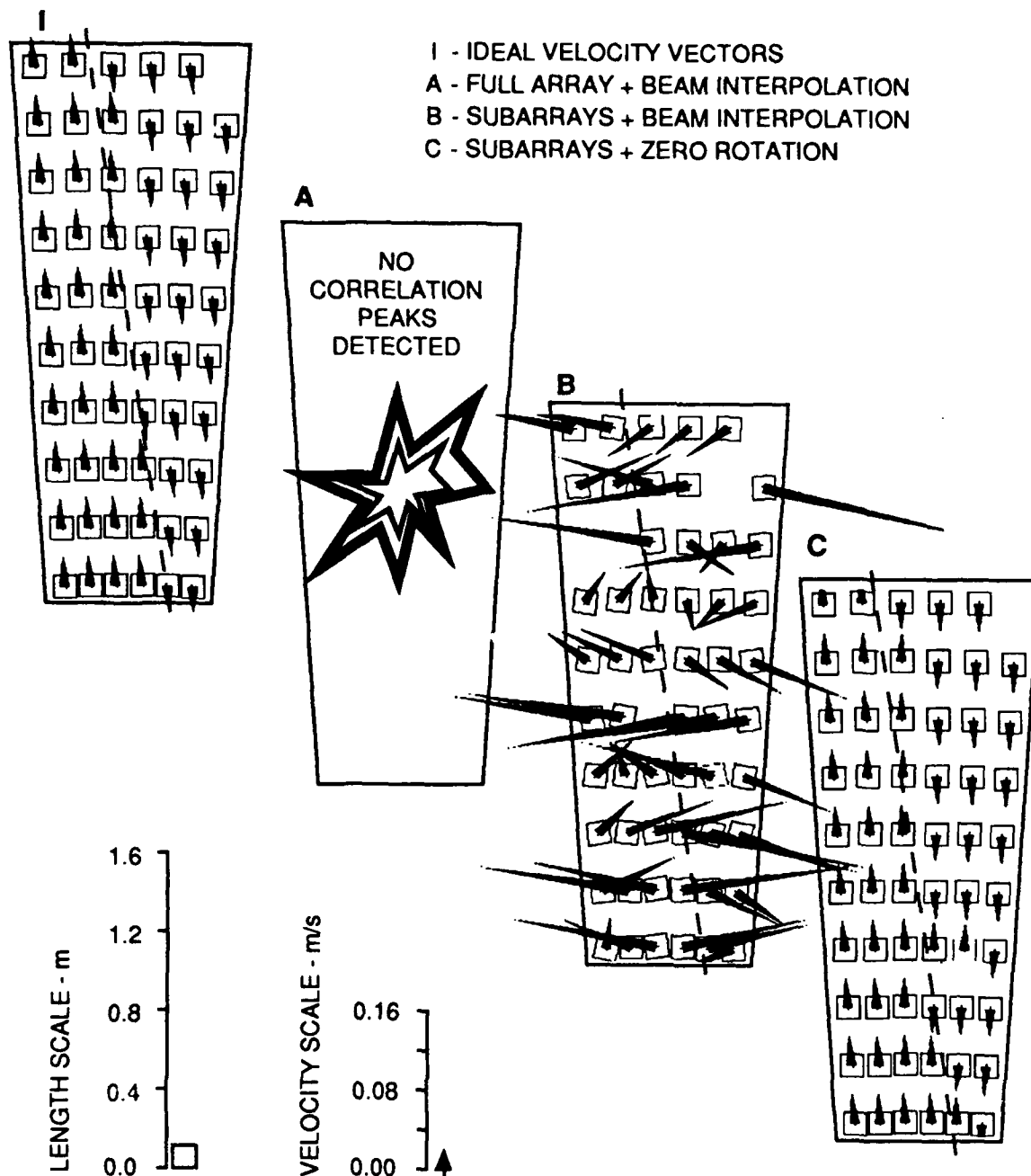B - SUBARRAYS + BEAM INTERPOLATION
C - SUBARRAYS + ZERO ROTATION
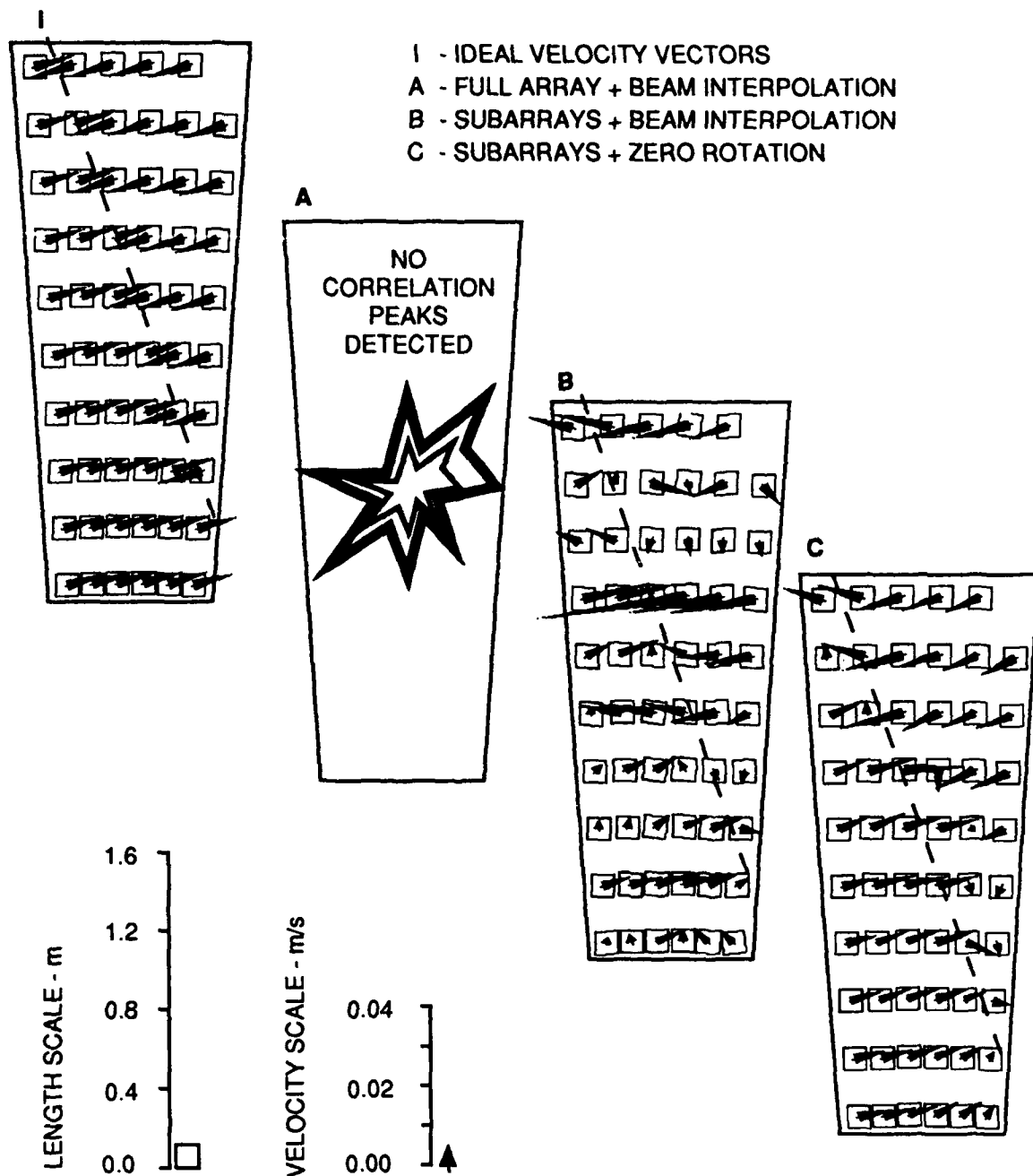
FIGURE 5.9
GRAPHICAL COMPARISON OF METHODS FOR A RANDOM SCATTERER FIELD
OF CONSTANT VELOCITY REGIONS
SEPARATED BY A PLANAR SINK BOUNDARY

LENGTH SCALE - m

FIELD OF VIEW

AZIMUTHALLY SHEARING
FIELD OF
RANDOM
SCATTERERS

Z

X

Y

TRANSDUCER
ARRAY
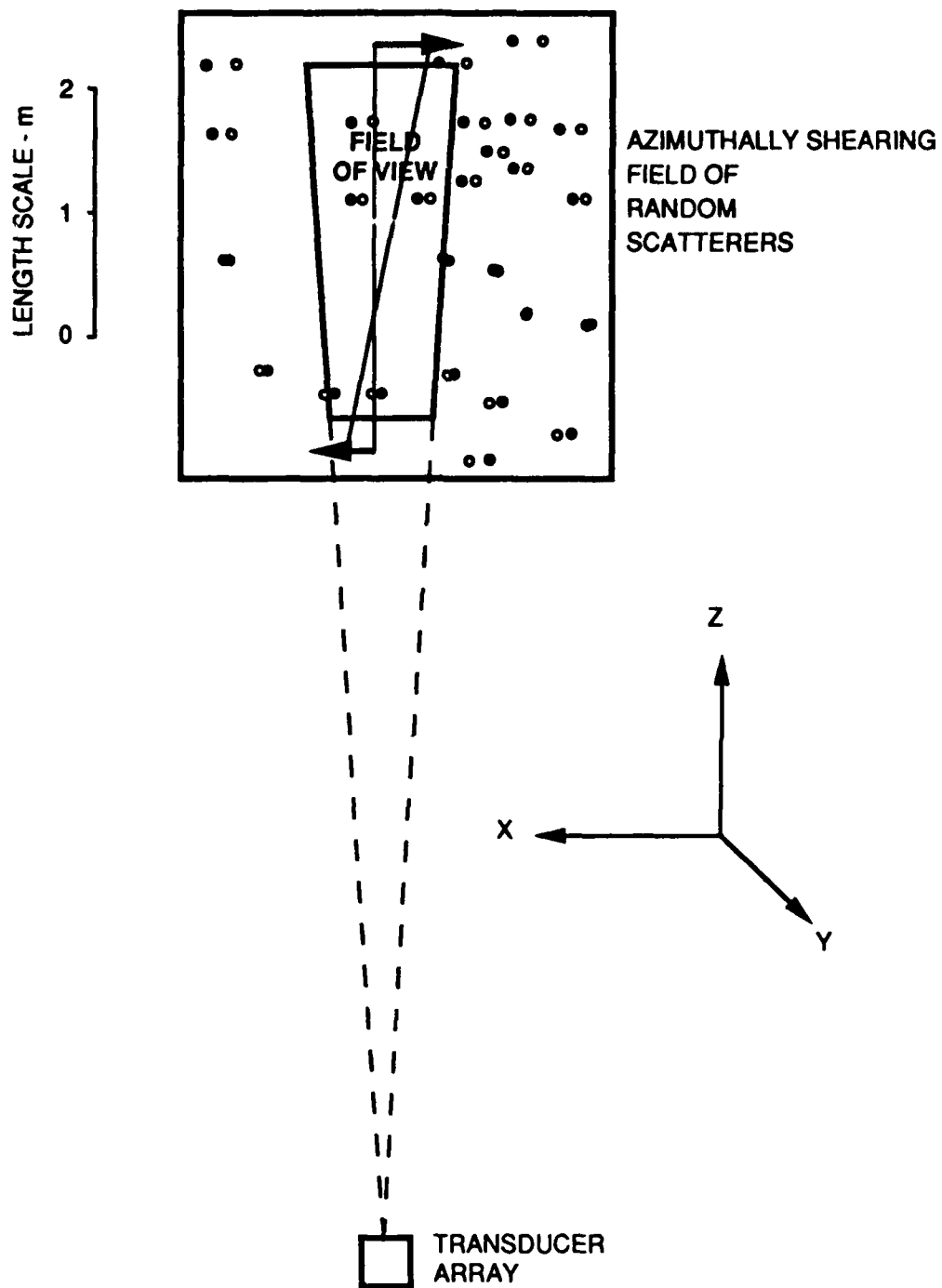
FIGURE 5.10
REMOTE SENSING SIMULATION OF A RANDOM SCATTERER FIELD
OF CONSTANT AZIMUTHAL SHEAR

I

I - IDEAL VELOCITY VECTORS
A - FULL ARRAY + BEAM INTERPOLATION
B - SUBARRAYS + BEAM INTERPOLATION
C - SUBARRAYS + ZERO ROTATION

A

NO
CORRELATION
PEAKS
DETECTED

B

C

LENGTH SCALE - m

1.6

1.2

0.8

0.4

0.0

VELOCITY SCALE - m/s

0.04

0.02

0.00
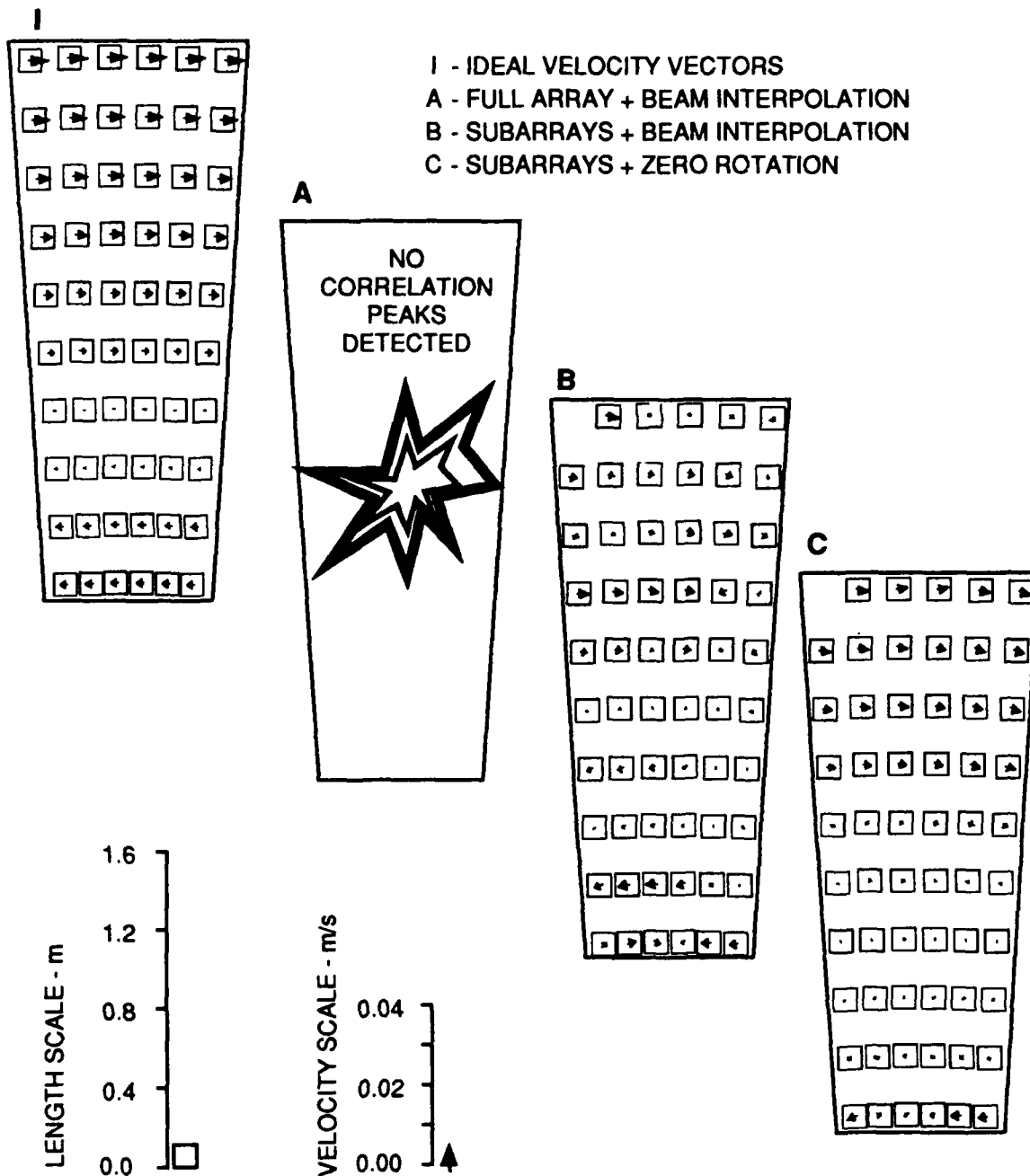
FIGURE 5.11
GRAPHICAL COMPARISON OF METHODS FOR A RANDOM SCATTERER FIELD
OF CONSTANT AZIMUTHAL SHEAR

39
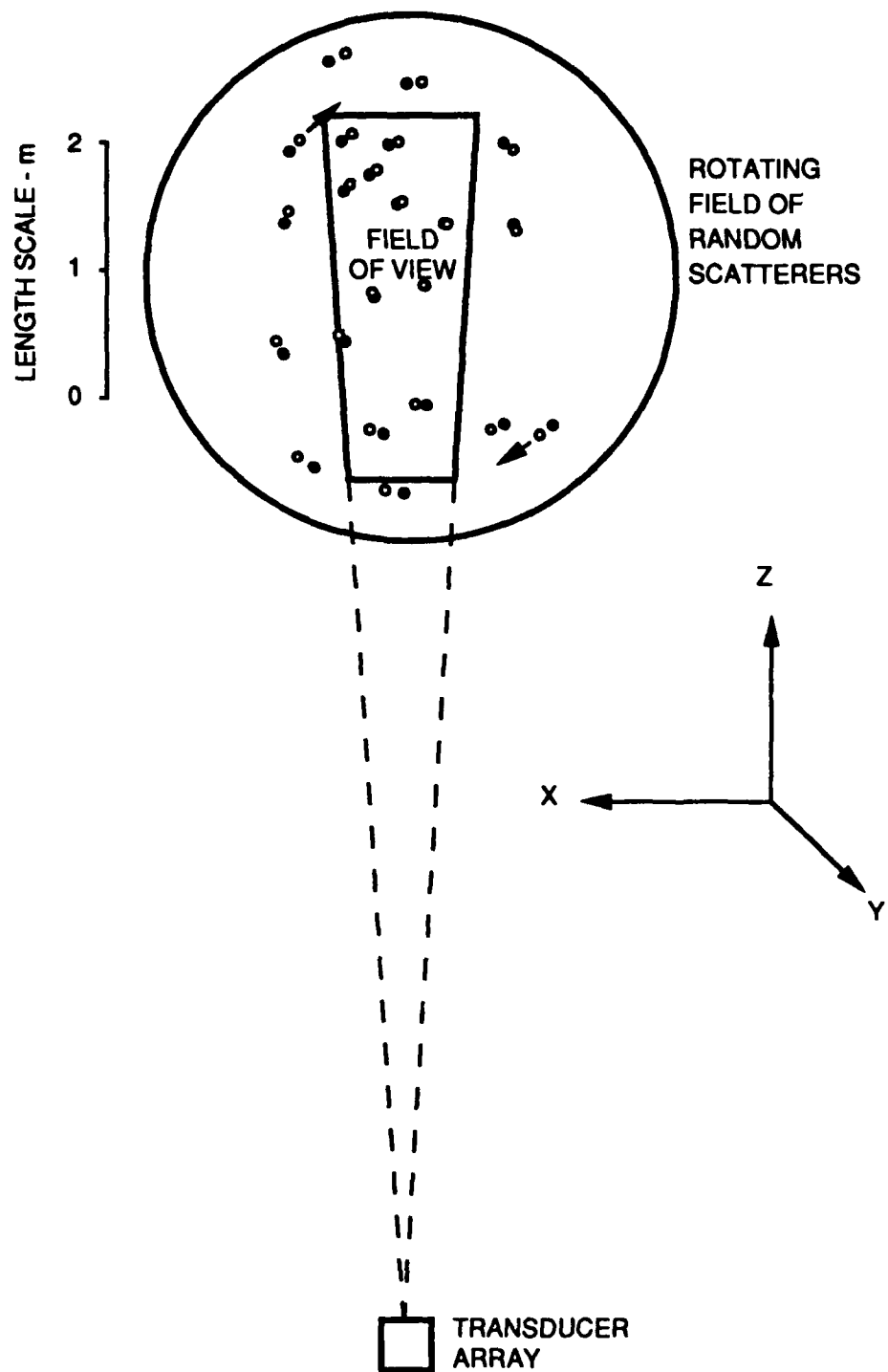
FIGURE 5.12
REMOTE SENSING SIMULATION OF A RANDOM SCATTERER FIELD
WITH CONSTANT ROTATION

I - IDEAL VELOCITY VECTORS
A - FULL ARRAY + BEAM INTERPOLATION
B - SUBARRAYS + BEAM INTERPOLATION
C - SUBARRAYS + ZERO ROTATION
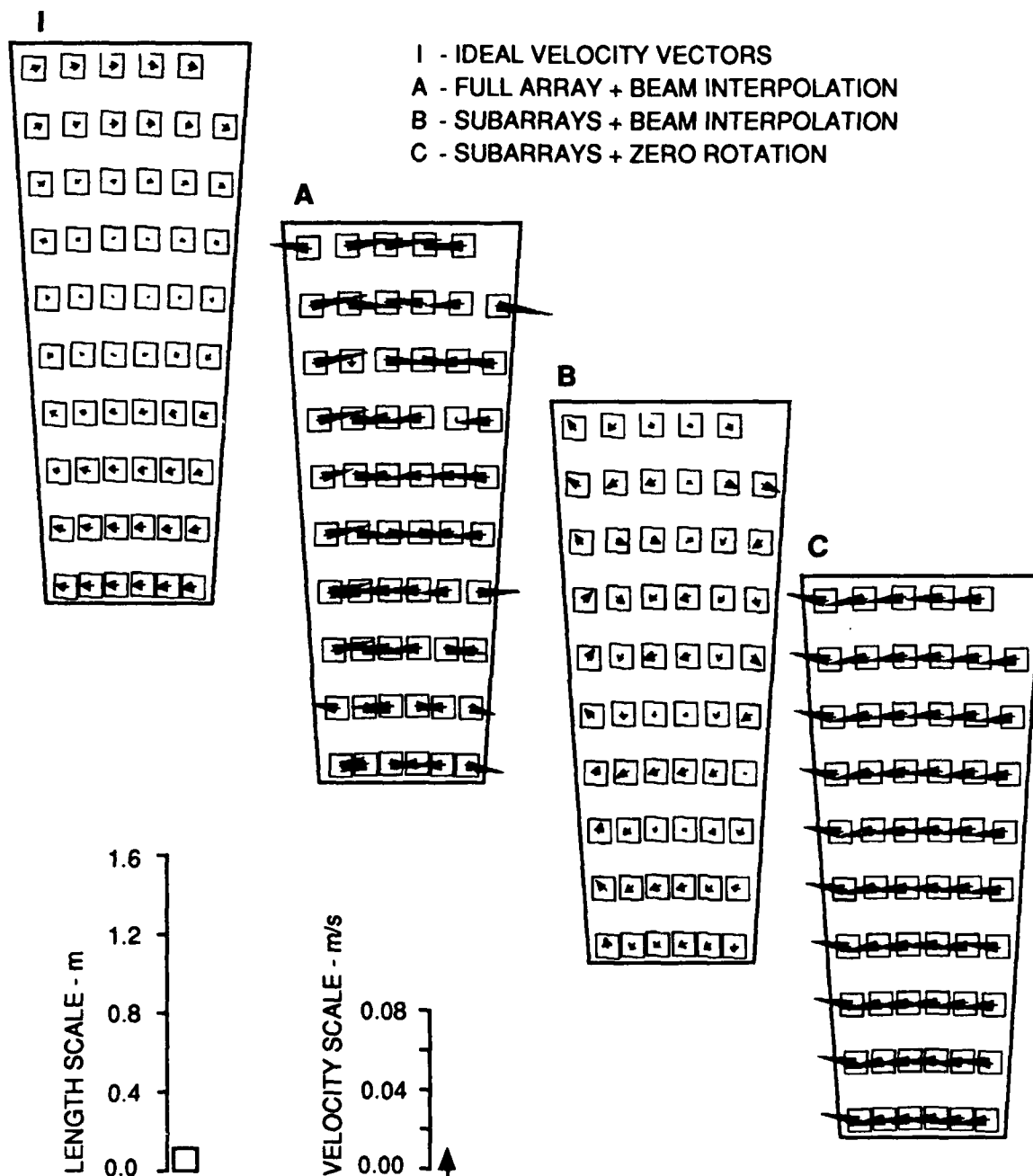
FIGURE 5.13
GRAPHICAL COMPARISON OF METHODS FOR A RANDOM SCATTERER FIELD
WITH CONSTANT ROTATION

5.7 CASE 7: CONSTANT RATE OF SHEAR IN THE AXIAL DIRECTION

The motion of the scatterers is illustrated in Fig. 5.14. The results obtained by the three methods are compared with the ideal result in Fig. 5.15. It was found that Method A was unable to obtain the minimum correlation peaks for displacement processing. It is seen that Method B produced results with gross errors in angular displacement. Method C gave results that were also quite wrong, indicating a right to left flow in addition to the shearing motion. The failure of Method C in this case is again due to the zero rotation assumption. Axial shear has the same effect on the lateral displacement of the backscatter signal as rotation. Therefore, Method C is quite inappropriate for this case.

At the stated ping repetition rate, a higher rate of shear caused the correlation peaks to be lost entirely, for the same reason as in the rotational case.
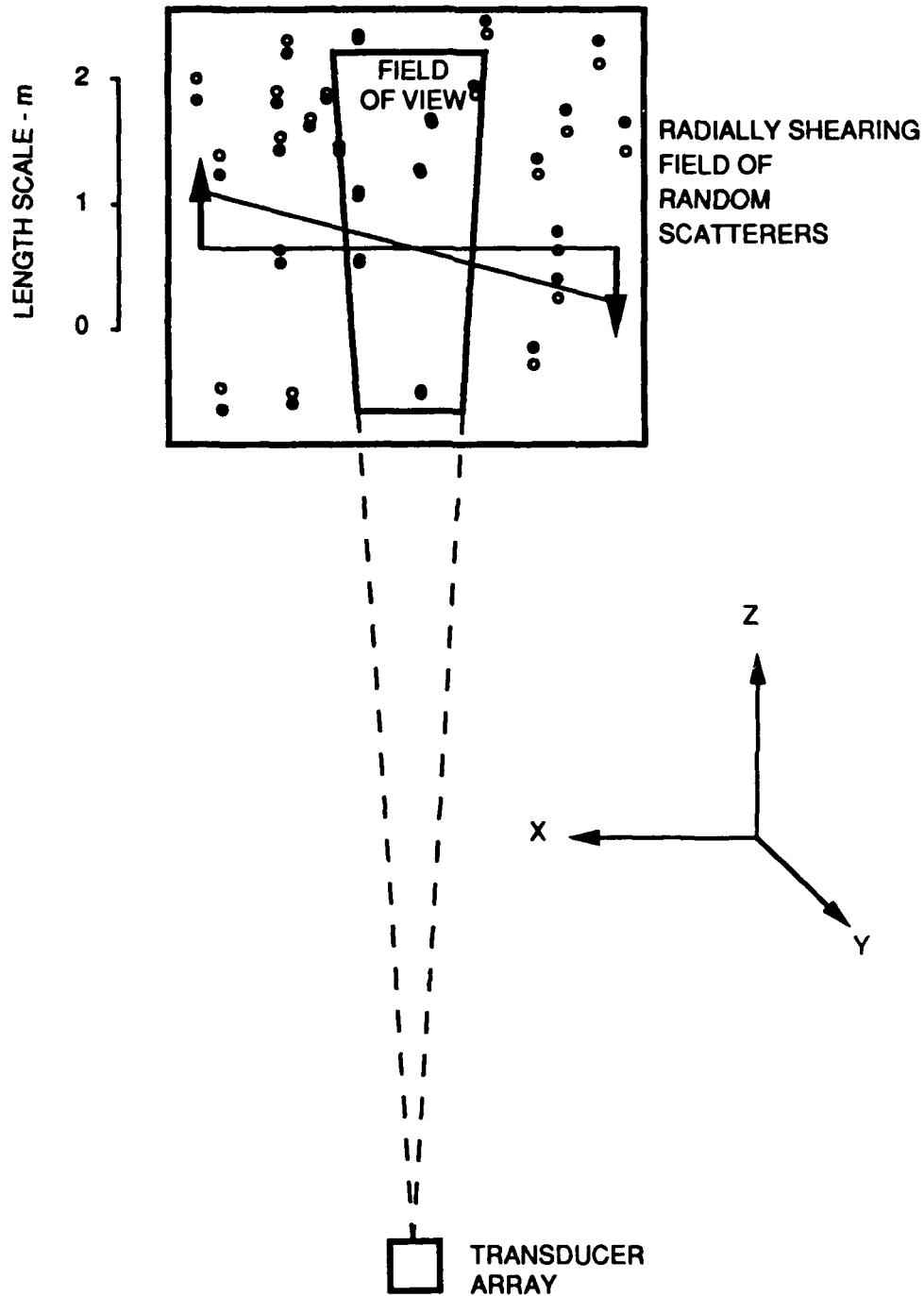
FIGURE 5.14
REMOTE SENSING SIMULATION OF A RANDOM SCATTERER FIELD
OF CONSTANT AXIAL SHEAR

43

I

I - IDEAL VELOCITY VECTORS
A - FULL ARRAY + BEAM INTERPOLATION
B - SUBARRAYS + BEAM INTERPOLATION
C - SUBARRAYS + ZERO ROTATION

A

NO
CORRELATION
PEAKS
DETECTED

B

C

LENGTH SCALE - m

1.6

1.2

0.8

0.4

0.0

VELOCITY SCALE - m/s

0.04

0.02

0.00
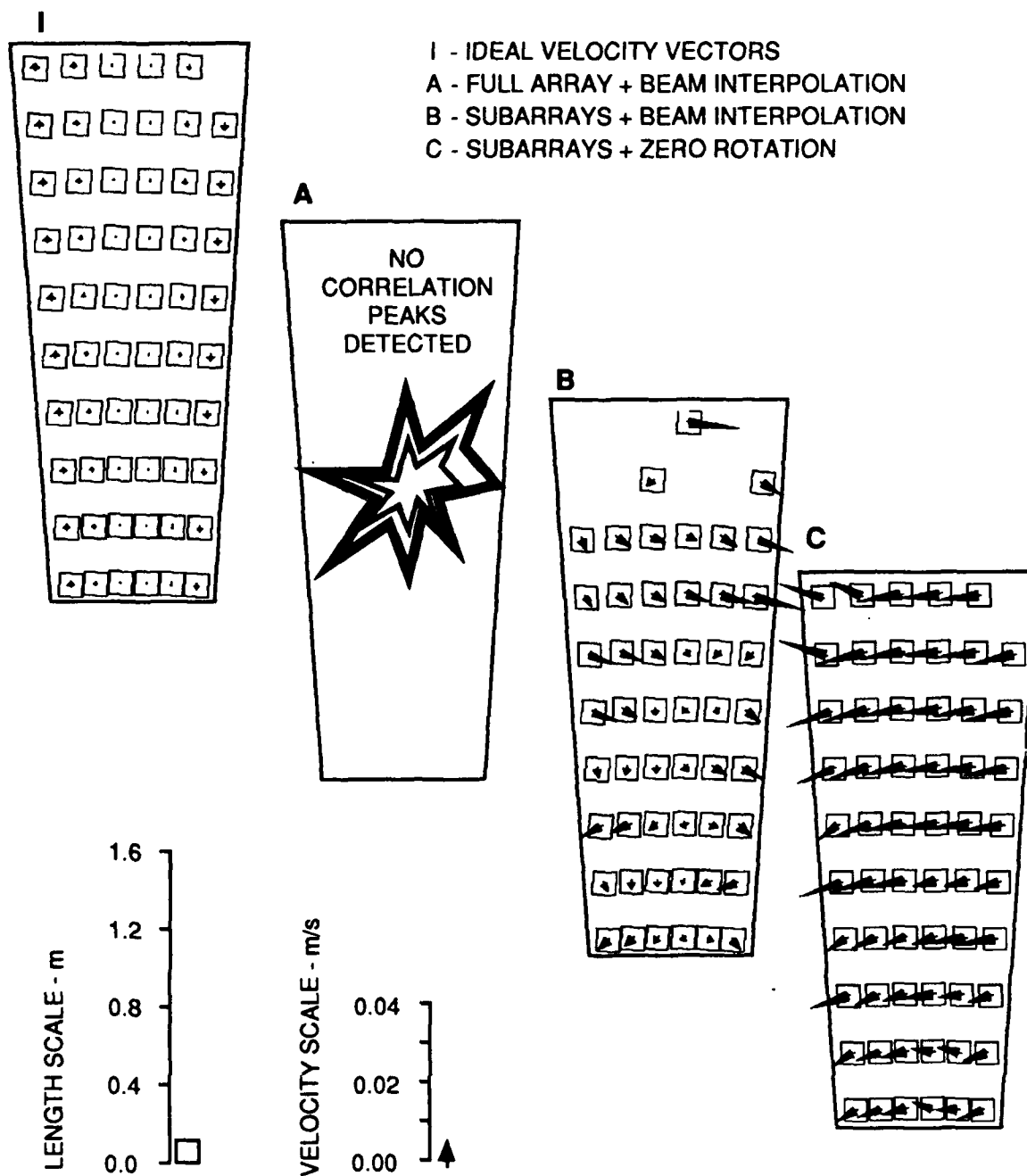
FIGURE 5.15
GRAPHICAL COMPARISON OF METHODS FOR A RANDOM SCATTERER FIELD
OF CONSTANT AXIAL SHEAR

6. ANALYSIS OF COMPUTER SIMULATION RESULTS

6.1 PERFORMANCE EVALUATION

The performance of the three methods in the above test cases are summarized in the form of error statistics in Tables 6.1 and 6.2. In each case, the estimated velocity is compared with the simulated velocity. The mean offsets and standard deviations of the difference were computed in m/s.

TABLE 6.1

AZIMUTHAL (x DIRECTION) VELOCITY ESTIMATION ERROR STATISTICS

	Method A		Method B		Method C	
Case	offset	standard deviation	offset	standard deviation	offset	standard deviation
1	0.002	0.019	-0.014	0.059	0.000	0.000
2	-0.004	0.019	-0.004	0.007	-0.002	0.002
3			-0.025	0.112	-0.001	0.003
4			-0.003	0.011	0.000	0.007
5			-0.008	0.013	-0.009	0.013
6			0.001	0.003	-0.017	0.003
7			0.002	0.004	-0.008	0.002

TABLE 6.2

AXIAL (z DIRECTION) VELOCITY ESTIMATION ERROR STATISTICS

	Method A		Method B		Method C	
Case	offset	standard deviation	offset	standard deviation	offset	standard deviation
1	-0.001	0.003	-0.001	0.003	-0.001	0.001
2	-0.001	0.001	-0.001	0.001	-0.001	0.001
3			0.000	0.016	0.002	0.015
4			0.000	0.001	0.000	0.002
5			-0.001	0.001	-0.001	0.001
6			-0.001	0.002	-0.001	0.002
7			-0.002	0.001	-0.002	0.002

The error statistics are also shown graphically, the error offsets in Fig. 6.1 and the error standard deviations in Fig. 6.2. With Method A and cases 3-7, correlation peaks were not detectable; therefore there were no applicable results. These cases are labeled "N/A".
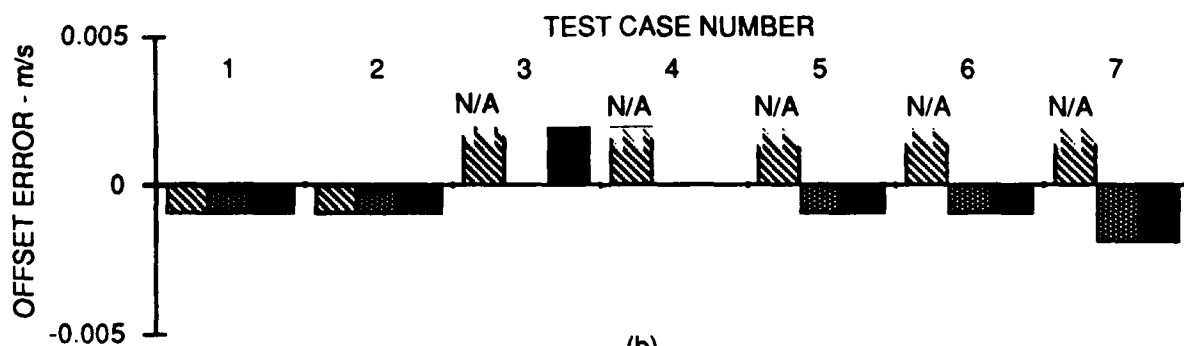
With regard to axial velocity errors, it is seen that the errors are small in all applicable cases. This is not surprising in view of the demonstrated successes of the pulse-to-pulse correlation and Doppler systems. The fact that the use of multi-subarrays in Methods B and C can recover the correlation peaks missed by the simple beamformer in Method A and thus allow the axial velocity to be measured is significant. This is demonstrated in cases 3-7. These results indicate that the accuracy and performance of pulse-to-pulse flow measurement systems can be improved by employing the multi-subarray method developed in this study.

With regard to the azimuthal velocity component, it is seen that Method C has the best performance in cases where the motion is irrotational, as demonstrated in cases 1-4. Furthermore, Melthod C is not confused by the presence of abrupt boundaries, as demonstrated in cases 3 and 4. Its main shortcoming is its inability to distinguish rotational motion from azimuthal translation as evidenced by the large offset errors in cases 5-7.

Although the offset errors of Method C were of similar magnitude for the shear and rotational test cases, as a fraction of the actual velocities, the offset for the azimuthal shear case (5) was significantly smaller than the other two cases (6 and 7). The reason is that the shear rate simulated in case 5 is three times greater than that in the other two cases. Therefore, it is deduced that Method C is less susceptible to azimuthal shear than either axial shear or rotation, and that Method C may still give fairly good results when used on flow fields that move mainly in the azimuthal direction. For example, shear layers may be observed using Method C if the sonar is directed perpendicularly to the layers.
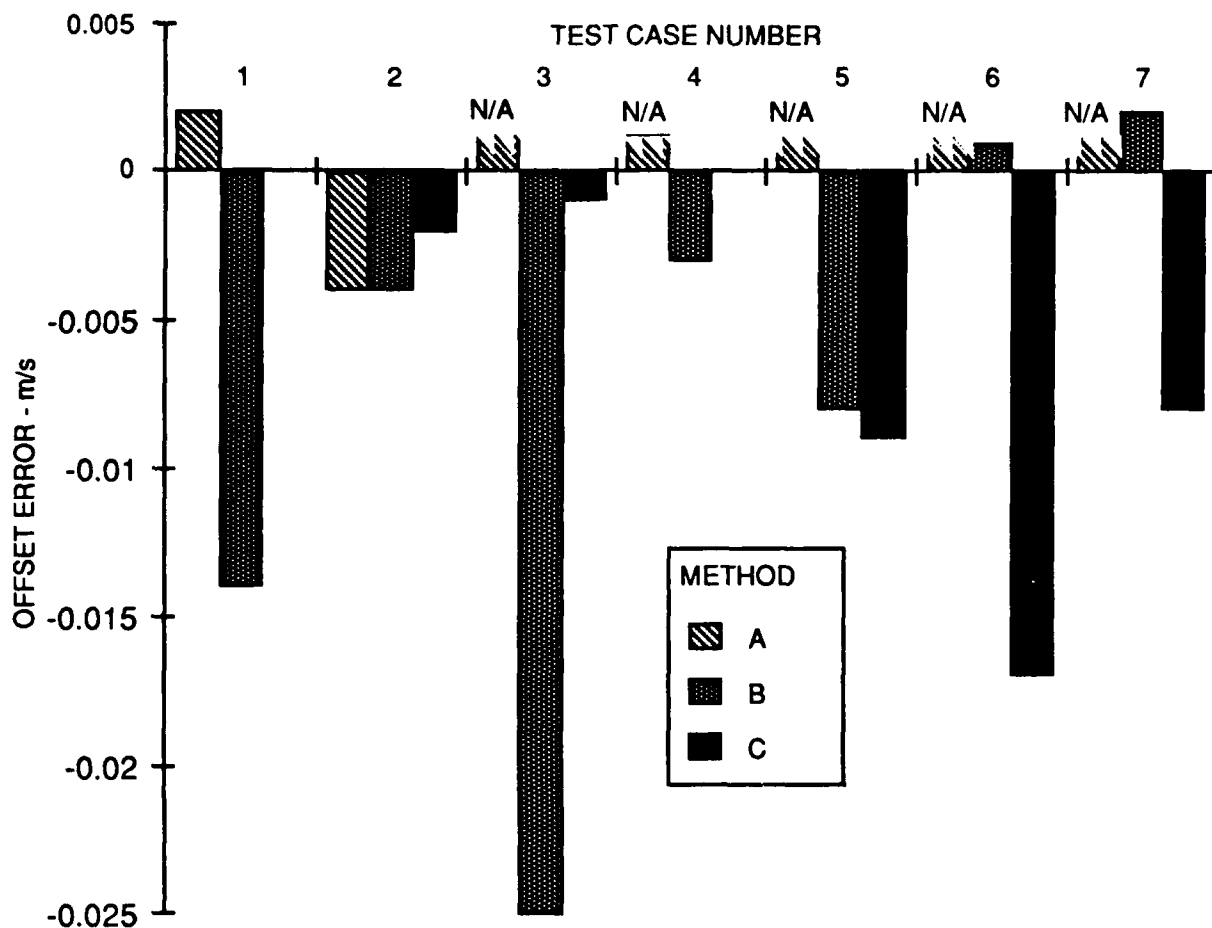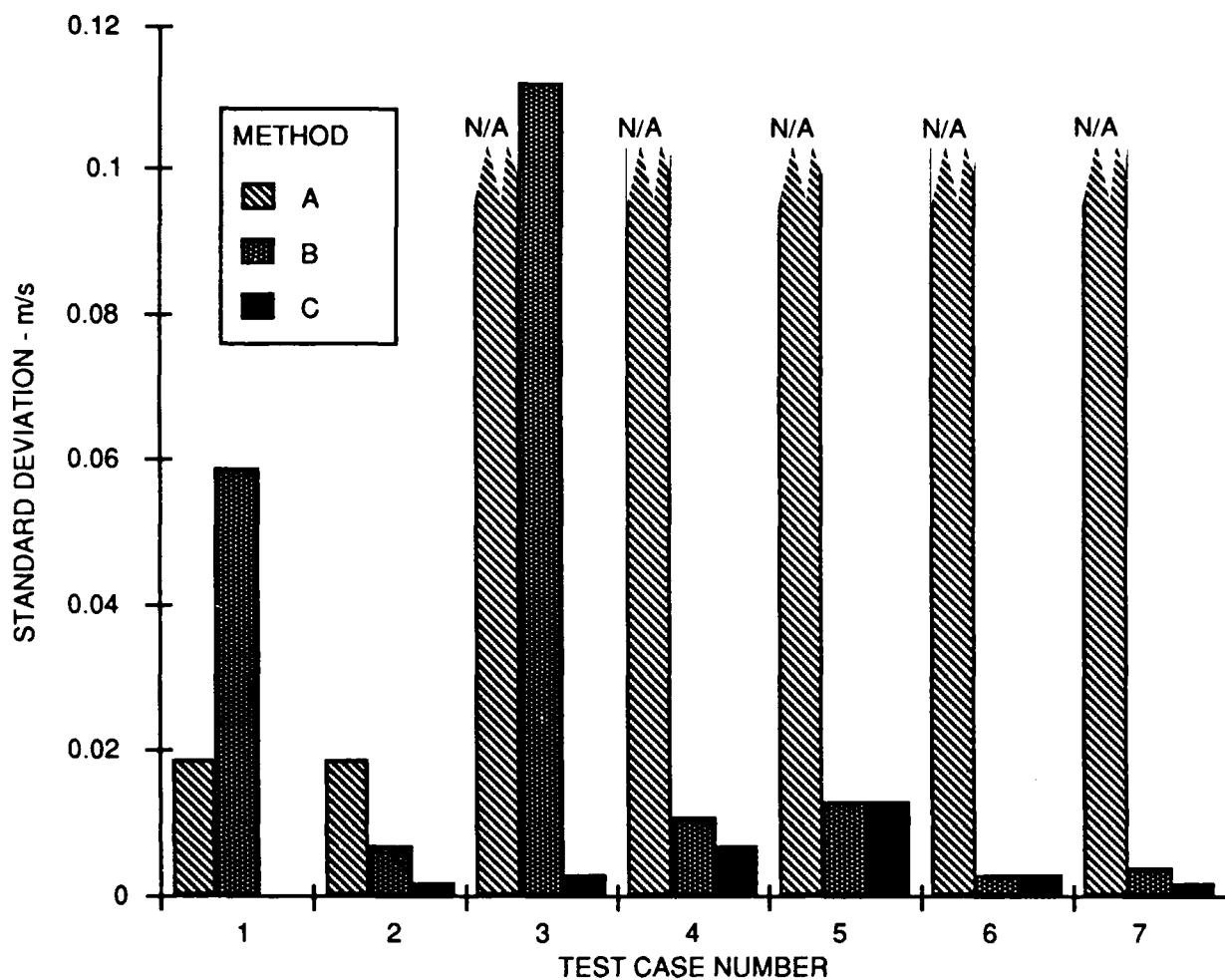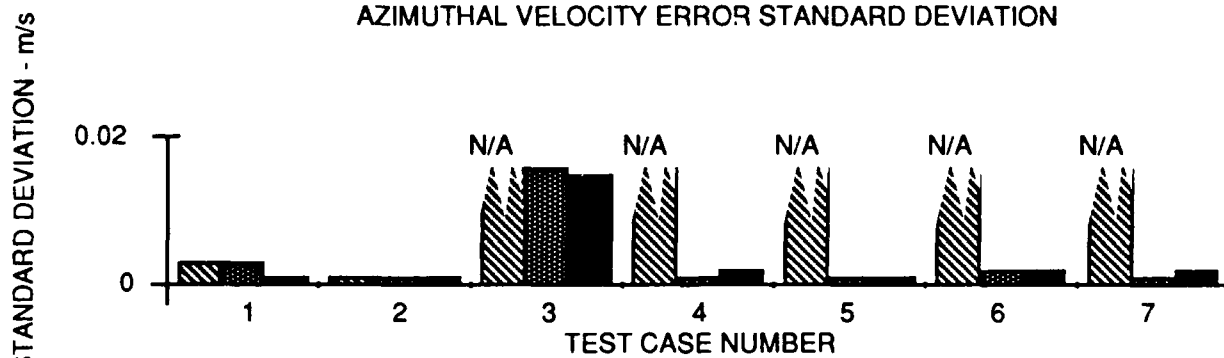
(a)
AZIMUTHAL VELOCITY ERROR OFFSET

(b)
AXIAL VELOCITY ERROR OFFSET

FIGURE 6.1
VELOCITY ERROR OFFSETS AS A FUNCTION OF TEST CASE AND METHOD

FIGURE 6.2
VELOCITY ERROR STANDARD DEVIATIONS
AS A FUNCTION OF TEST CASE AND METHOD

48

6.2 ABSENCE OF A DISCERNIBLE WAVEFRONT

The failure of Methods A and B in all cases indicates that there is minimal coherence across the backscattered wavefront. From these results, it should be concluded that there is no wavefront at all. The reason for the less-than-cooperative behavior of the backscatter signature becomes apparent when the dimensions of the scatterer cloud are taken into account. Assuming that the cloud is in the farfield of the hydrophone, the azimuthal extent of the cloud is determined by the beamwidth of the hydrophone. With a beamwidth θ, at a range r, the diameter of the cloud is simply θr. Thus, the backscattered signal may be considered as a signal projected from an aperture of the same diameter. At an acoustic wavelength λ, the Rayleigh distance R_c of such a source is approximately given by

$$R_c = (\theta r)^2/\lambda \quad .$$

(6.1)

In order to have properly formed beams, the cloud must be in the farfield of the hydrophone. Therefore we have the inequality

$$r < d^2/\lambda \quad ,$$

(6.2)

where d is the diameter of the hydrophone and related to the beamwidth by

$$\theta = \lambda/d \quad .$$

(6.3)

Eliminating θ, λ, and d from the above equations, we obtain the important result

$$R_c > r \quad .$$

(6.4)

That is, the hydrophone is always in the nearfield of the backscattered signal.

The above analysis explains the absence of coherent wavefronts and the poor performance of algorithms based on wavefront estimation, particularly beam interpolation. The acoustic backscatter signatures are more appropriately described as speckle patterns that vary as a function of the relative positions and orientations between the projector, scatterer cloud, and hydrophone. Therefore,

49

orientations between the projector, scatterer cloud, and hydrophone. Therefore, azimuthal motion estimation should not be approached as a beamforming or beam interpolation problem. Instead, it should be approached as a problem of interpreting speckle pattern migrations.

7. EXPERIMENTAL RESULTS

To demonstrate the acoustic remote sensing of three-dimensional motion, it would have been necessary to construct a planar array with many elements--at least 30. To minimize costs, a small line array was used, thus limiting the scope of the feasibility demonstration to two-dimensional motion problems.

The construction of the hardware will be briefly described. Initial experiments using an array of discrete parallel beams are briefly mentioned. The main experiments using a continuous line array, both in the laboratory tank and in the field, are then described with examples of the results obtained.

7.1 HARDWARE

The data acquisition system consisted of a D/A converting and sampling unit from DSP Technology, Inc., controlled by an Apple Macintosh II computer using the LabVIEW virtual instrument software from National Instruments, Inc. A schematic of the system is shown in Fig. 7.1.

A projector was designed by Reuben Wallace and built in the ARL:UT transducer workshop to operate at a center frequency of 200 kHz, with a minimum bandwidth of 60 kHz. A diagram of the projector is shown in Fig. 7.2. The active material is a 5500 type ceramic.

An array of six hydrophones, matching preamplifiers, cables, and receiver electronics were designed and constructed using PVdF tiles mounted on steel backing plates. PVdF was chosen for its wideband capability. A photograph of the units is shown in Fig. 7.3.

7.2 PARALLEL BEAM EXPERIMENTS

We had the option of either constructing a line array on one PVdF tile or using all six tiles to form an array of parallel beams. We ended up doing both. We started with the option of using parallel beams because, from a practical point of

FIGURE 7.1
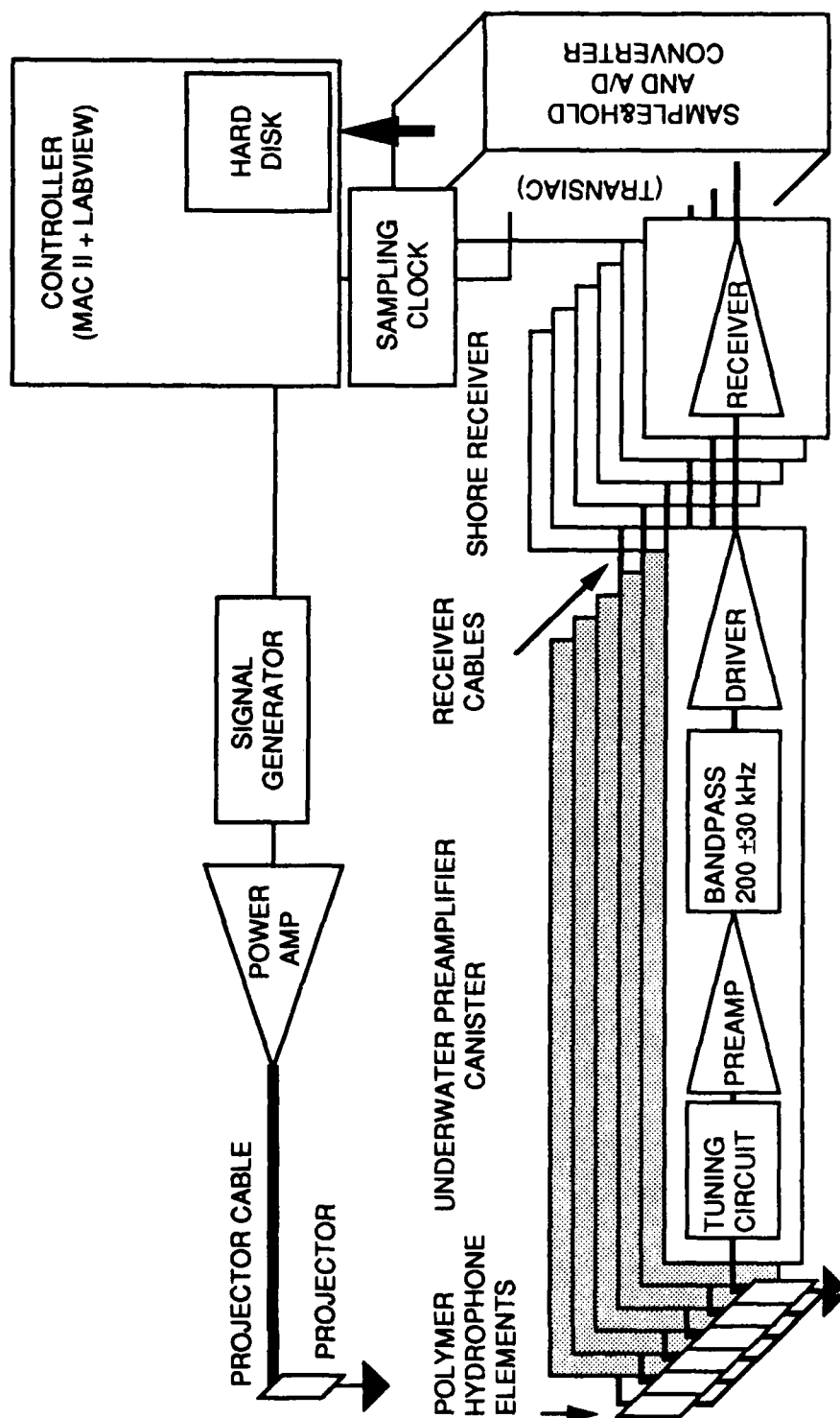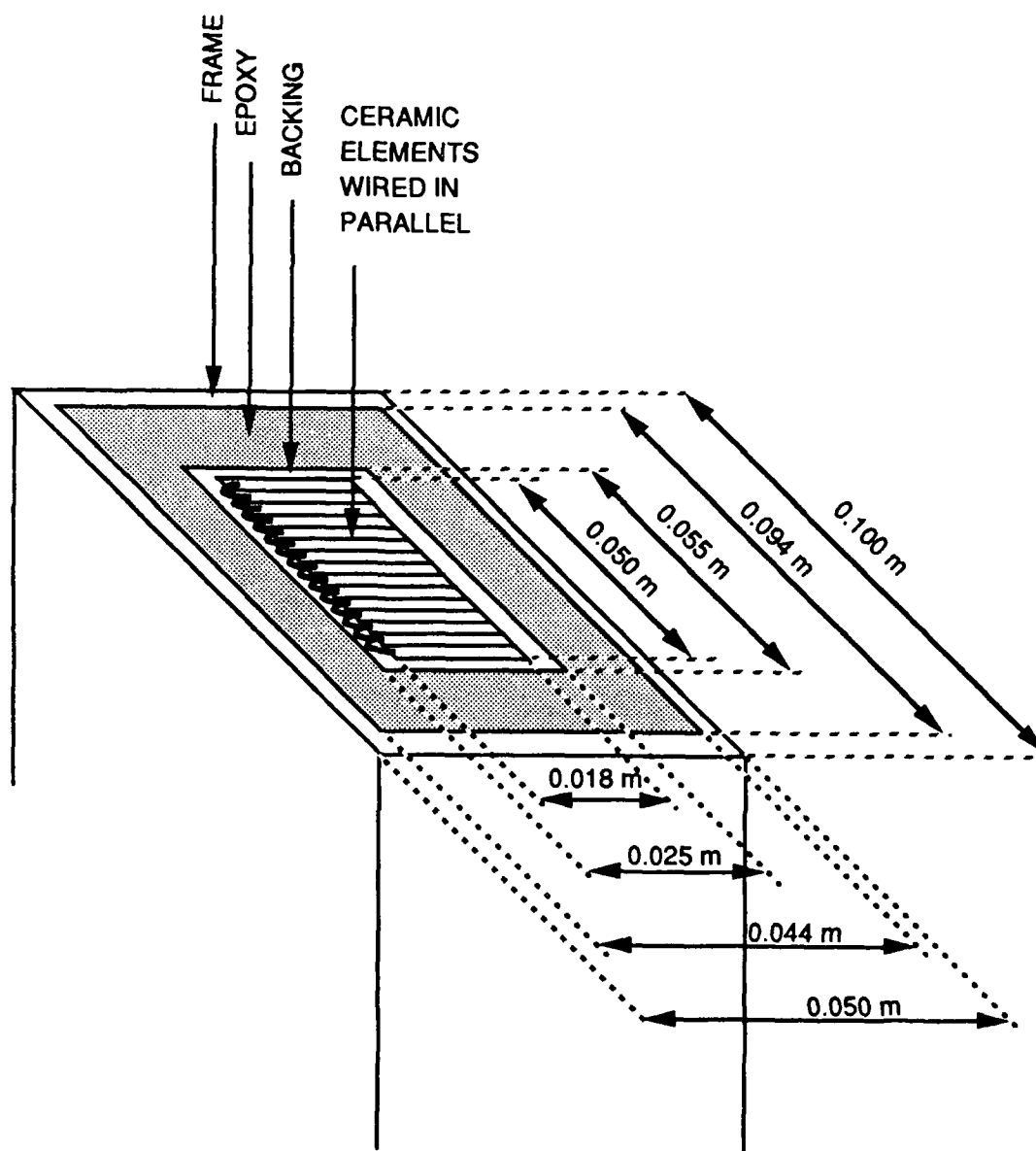
SCHEMATIC OF SONAR AND DATA ACQUISTION SYSTEM

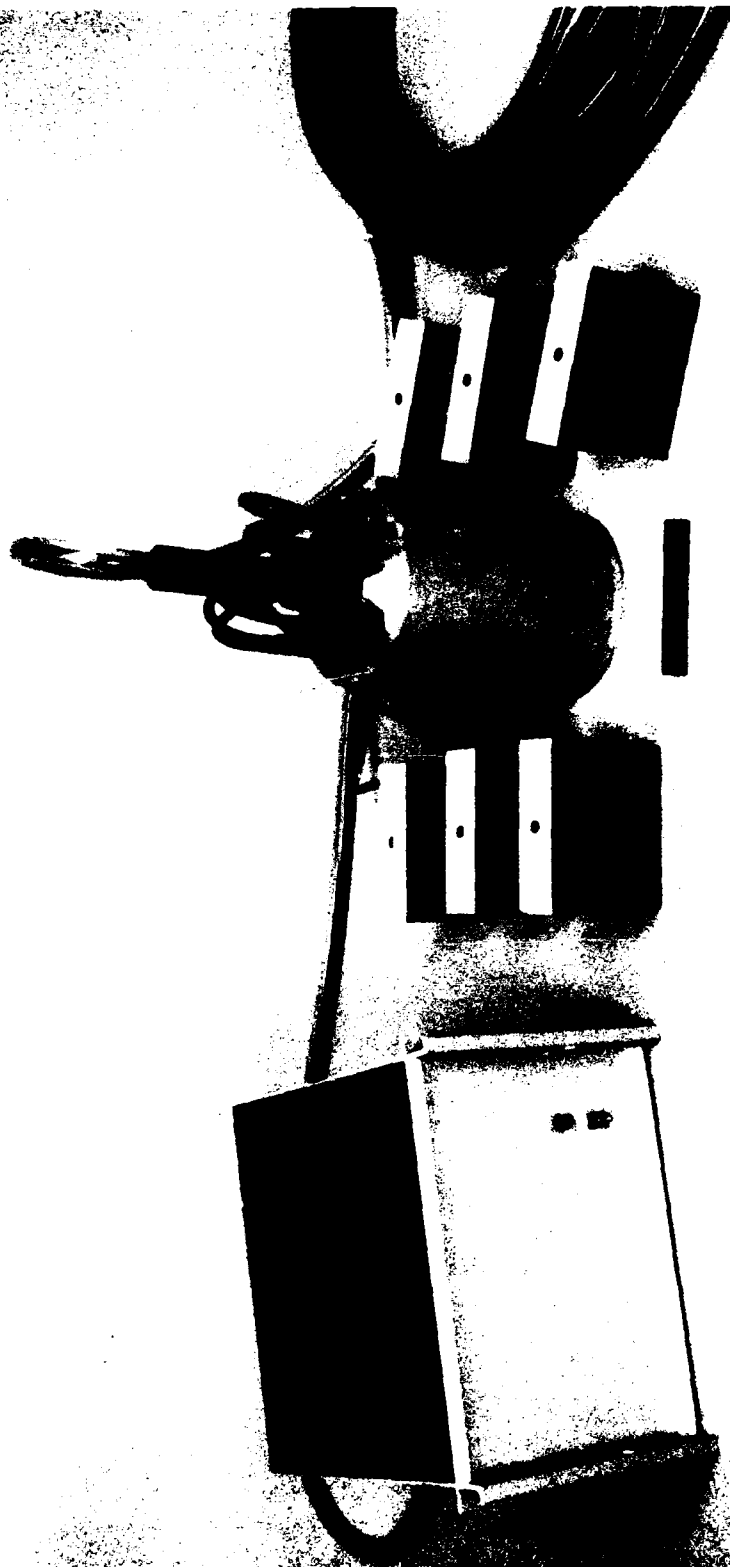**FIGURE 7.2**
DIAGRAM OF THE PROJECTOR

FIGURE 7.3
PHOTOGRAPH OF THE RECEIVE SYSTEM COMPONENTS, INCLUDING SHORE RECEIVER, PVdF ELEMENTS, PREAMPLIFIER CANISTER, AND CABLE

5325-1

view, it was the simplest. The PVdF tiles were arranged in a line to give six parallel beams 20 cm apart. This configuration had the practical advantage of not requiring any beamforming in the processing software. The beams overlapped to allow interpolation methods to be used to determine fractional displacements in the azimuth direction. The main limitation was that only Method A was compatible with this arrangement. It turned out that this limitation was crucial. The computer simulation results, supported by laboratory experiments using the parallel beams arrangement, indicated that Method A was inappropriate. The experiments, described in an earlier letter report,[10] were carried out with backscatter from a rough concrete wall moving at a known speed relative to the sonar. Therefore, the parallel beam arrangement was abandoned.

7.3 CONTINUOUS LINE ARRAY EXPERIMENTS

A PVdF tile was divided into a line array of six elements, as shown in Fig. 7.4. The front electrode was scored to provide six separate electrodes, giving six elements with a common back electrode. The signals from each element were recorded and processed according to the methods described in Section 4. The geometry is identical to that of the computer simulated system shown in Fig. 3.1.

7.3.1 Tank Experiments

Experiments were carried out in one of the indoor tank facilities at ARL:UT. The tank measurements are 18 m long by 4.5 m wide by 3.3 m deep.

Experiments were made with backscatter from a rough concrete tank wall. The sonar was moved at a known speed relative to the wall, as illustrated in Fig. 7.5. From the point of view of the sonar, the wall appeared to move in the azimuth direction (x direction). The results are shown in Fig. 7.6. It is seen that Methods A and B gave grossly erroneous estimates of velocity. Method C gave estimates that were in very good agreement with the known velocity of the wall. These results are also very similar to those obtained with simulated data for the corresponding test case 2.

Experiments were made with a stream of hydrogen bubbles, rising from a wire at the bottom of the tank. The bubbles were produced by passing a dc
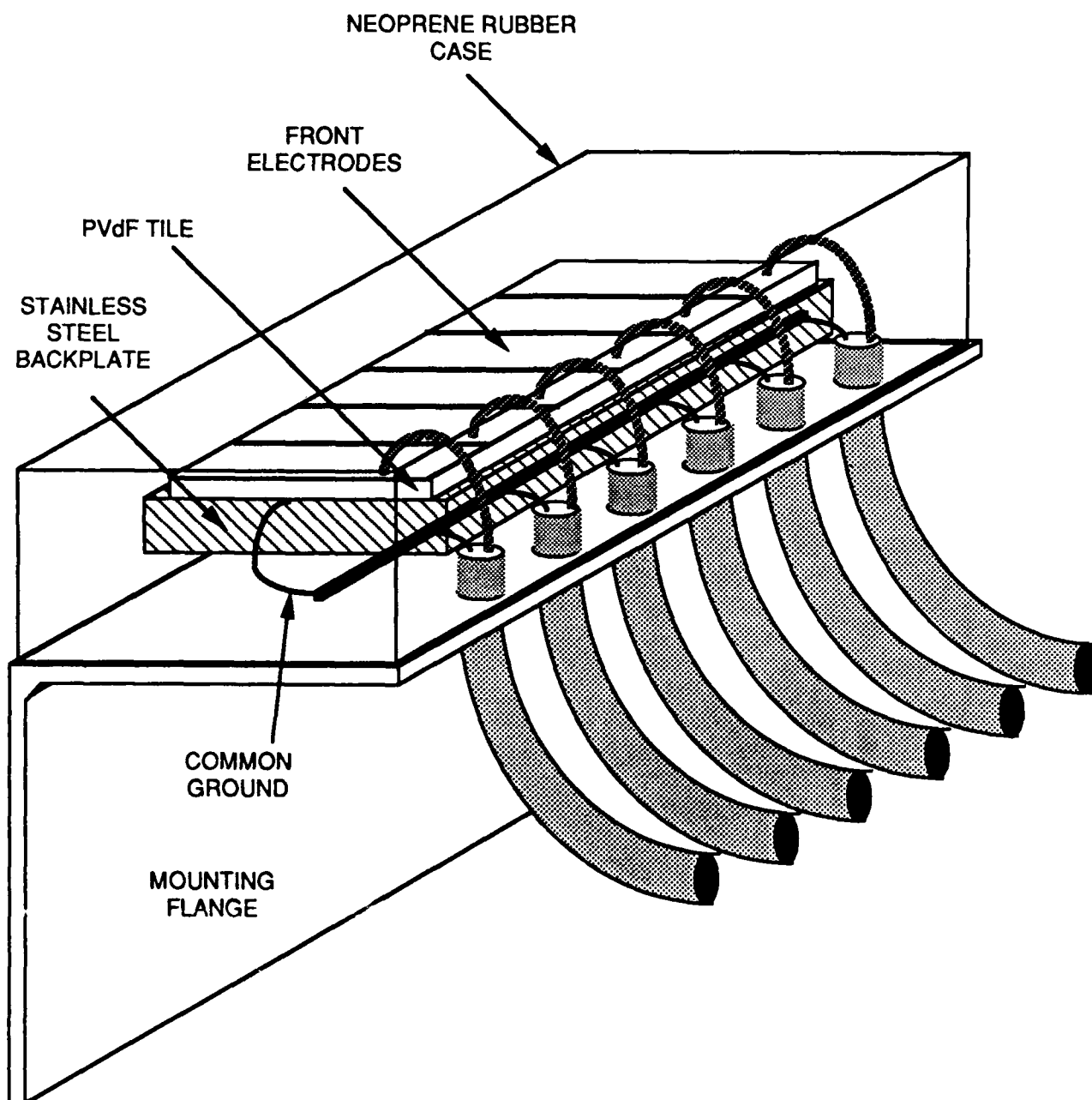
FIGURE 7.4
CONTINUOUS HYDROPHONE LINE ARRAY

NEOPRENE RUBBER
CASE

FRONT
ELECTRODES

PVdF TILE

STAINLESS
STEEL
BACKPLATE

COMMON
GROUND

MOUNTING
FLANGE
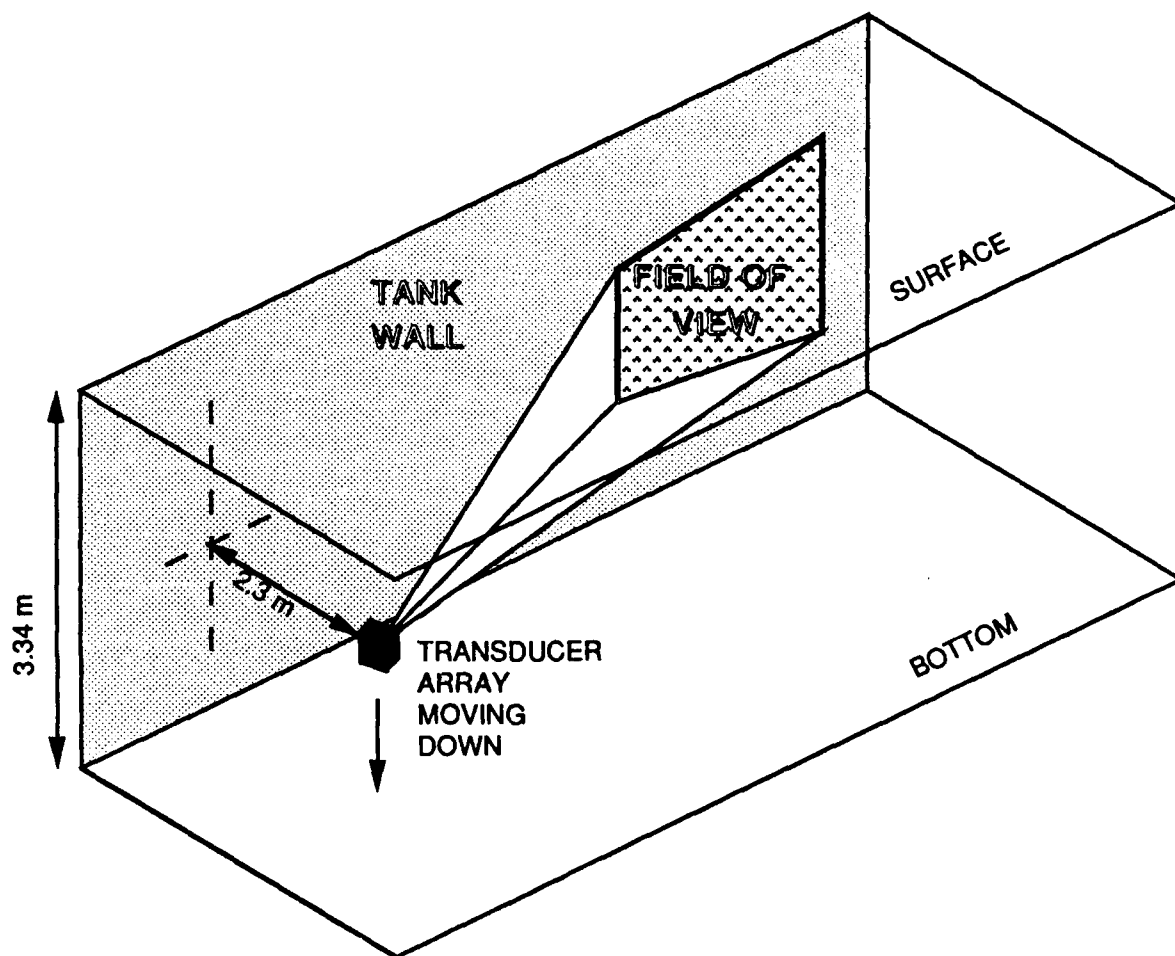
FIGURE 7.5
MOVING WALL EXPERIMENT WITH CONTINUOUS LINE
ARRAY

I - IDEAL VELOCITY VECTORS
A - FULL ARRAY + BEAM INTERPOLATION
B - SUBARRAYS + BEAM INTERPOLATION
C - SUBARRAYS + ZERO ROTATION

FIGURE 7.6
RESULTS OF MOVING WALL EXPERIMENT WITH CON⋅INUOUS LINE ARRAY

ARL:UT
AS-89-104
NPC - DS
3-2-89

58

current to the wire through the water from a separate anode, with a 50 V 10 A power supply. There was sufficient ionization in the water to allow the release of hydrogen gas at the wire cathode without adding any electrolyte.

Experiments were made with the sonar beam directed horizontally across the bubble stream. Thus, the bubbles were moving in the azimuth direction (x direction) from the point of view of the sonar, as shown in Fig. 7.7. The bubble field contained bubbles of a variety of sizes, each rising at its own terminal velocity. Although the bubbles are generally moving up towards the surface, there were also large random velocity components which could not be precisely known or measured. Simple timing measurements between the start of bubble generation and the first bubble arrivals at the surface indicated that the mean velocity was in the region of 2 cm/s. The results obtained are shown in Fig. 7.8. It is seen that Method A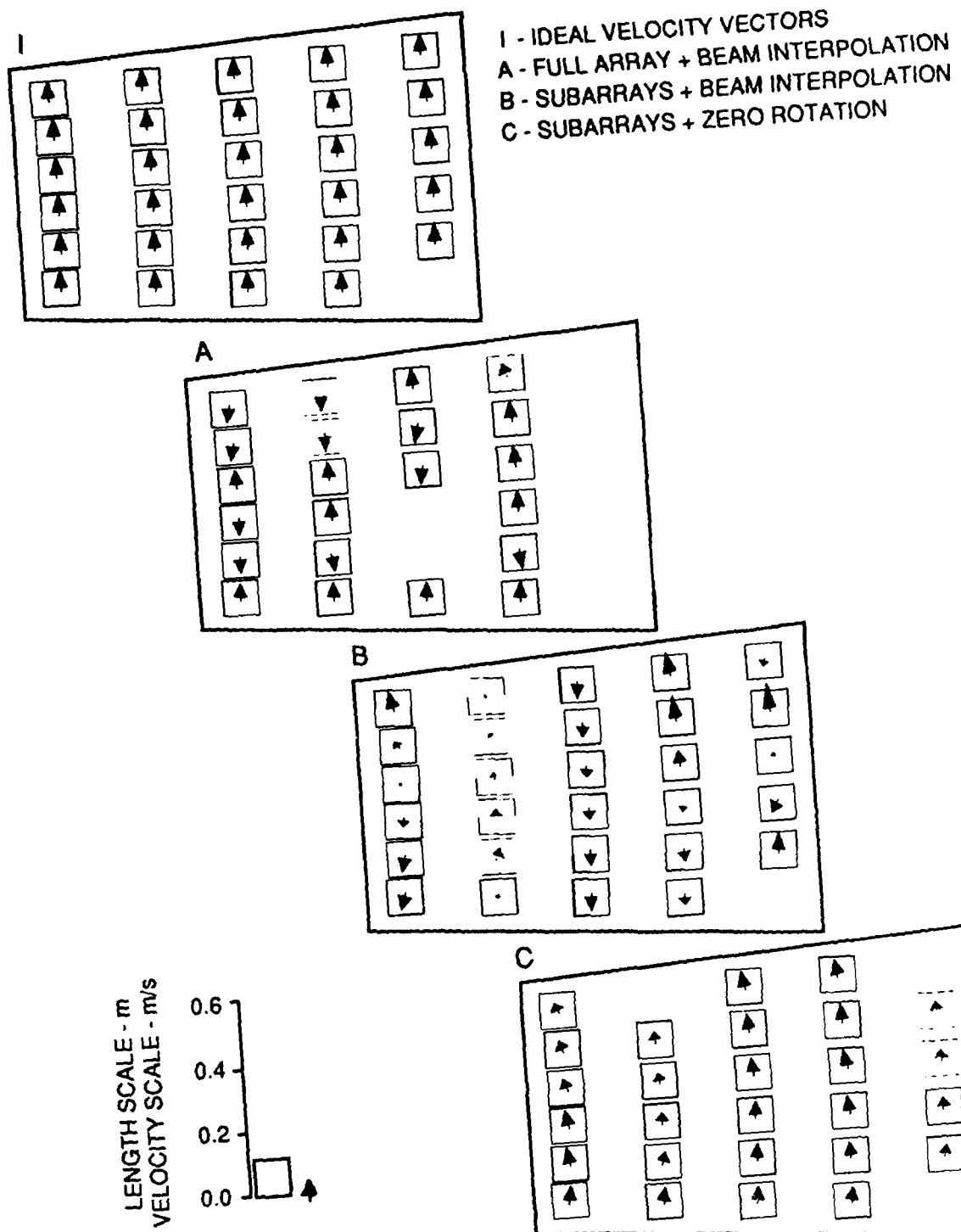 was quite unable to find any correlation peaks. Method B gave grossly erroneous results. Method C gave results which appear to be not unreasonable; the velocity vectors indicate rising motion at the correct mean velocity. The velocity field was constantly changing with time and we were unable to determine if the results given by Method C exactly matched the true field at all points and at all times.

In another experiment, the sonar was positioned on the tank bottom looking up into the bubble stream as shown in Fig. 7.9. The sonar beam intersects the bubble stream at a point near the water surface and is reflected back into the bubble stream by the surface. The results are shown in Fig. 7.10. It is expected that the bubble stream will be seen moving away from the sonar and then, beyond the surface, a reflection of the bubble stream moving towards the sonar. It is seen that Method A failed to detect any correlation peaks. Method B gave curiously erroneous results. Method C gave results that were not unreasonable. The reflected image of the bubble stream above the water surface in Method C was in fact rather unstable; it would change direction from time to time, probably due to modification of the image velocity by the surface motion.

Attempts were made to modify the bubble flow field with a water jet. It was found, however, that the shear stresses produced by the jet caused too much rotational motion and unwanted movement in the y direction for the experimental two-dimensional system to function properly.

**FIGURE 7.7
EXPERIMENT WITH BUBBLE STREAM IN THE AZIMUTH
DIRECTION**

I - IDEAL VELOCITY VECTORS
A - FULL ARRAY + BEAM INTERPOLATION
B - SUBARRAYS + BEAM INTERPOLATION
C - SUBARRAYS + ZERO ROTATION

FIGURE 7.8
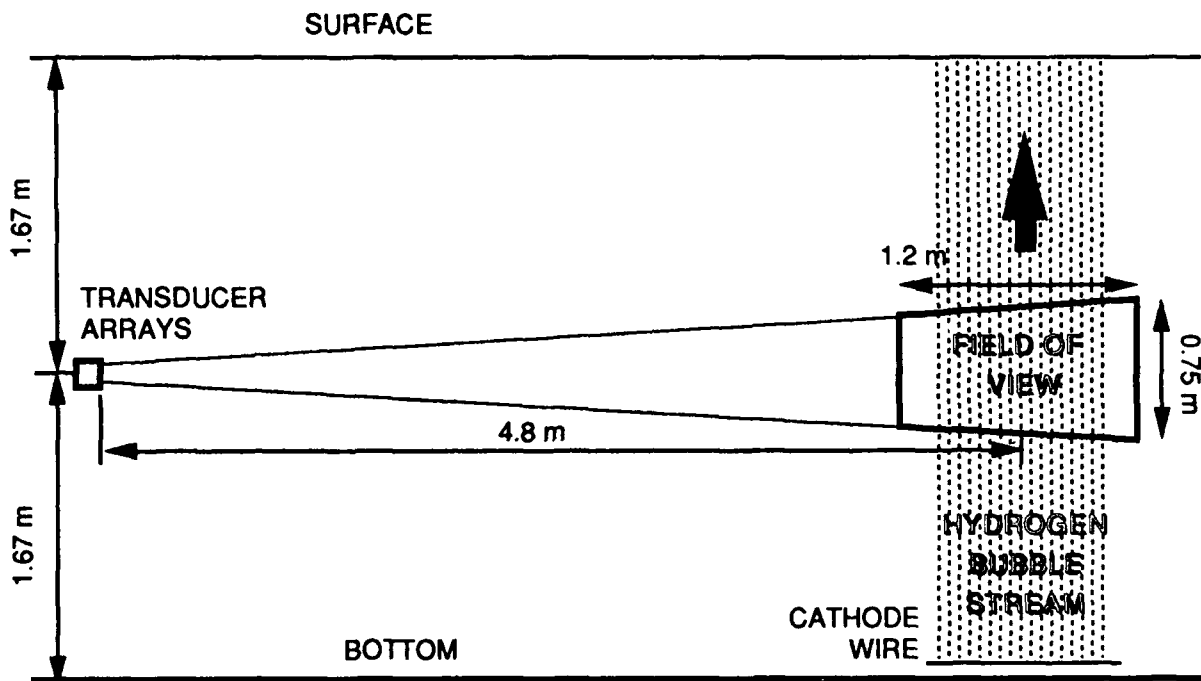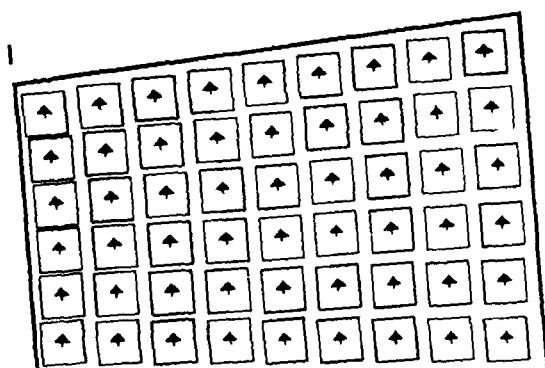**RESULTS FROM BUBBLE STREAM IN THE AZIMUTH DIRECTION**
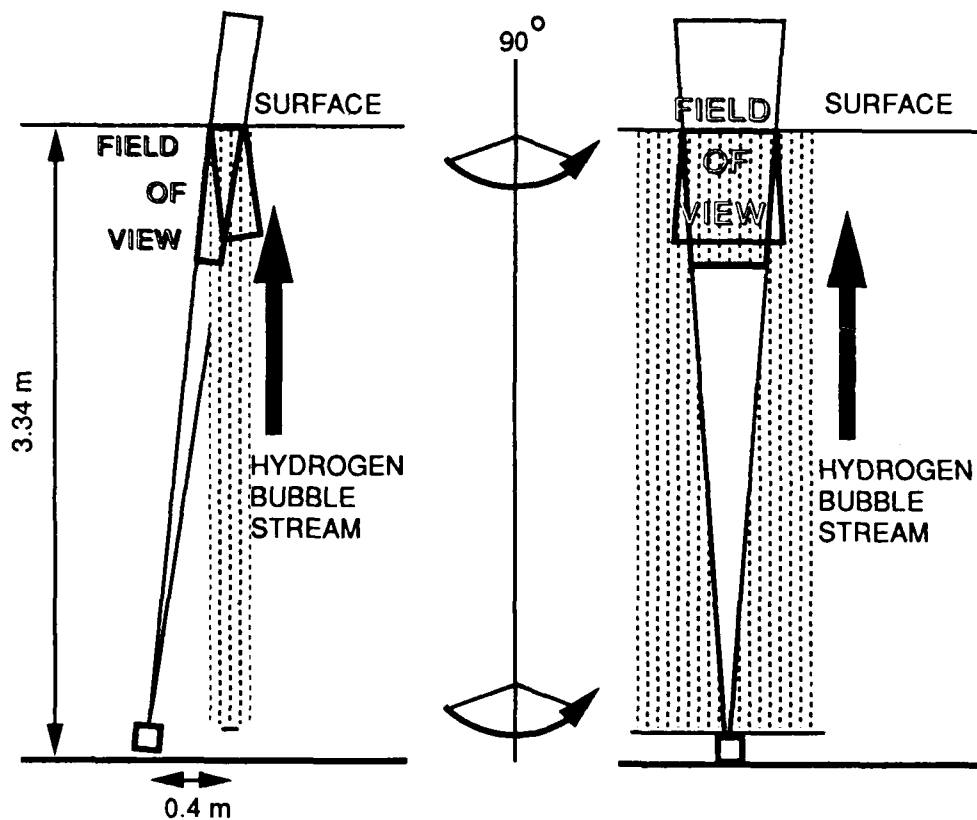
FIGURE 7.9
EXPERIMENT WITH BUBBLE STREAM IN THE AXIAL DIRECTION

I - IDEAL VELOCITY VECTORS
A - FULL ARRAY + BEAM INTERPOLATION
B - SUBARRAYS + BEAM INTERPOLATION
C - SUBARRAYS + ZERO ROTATION

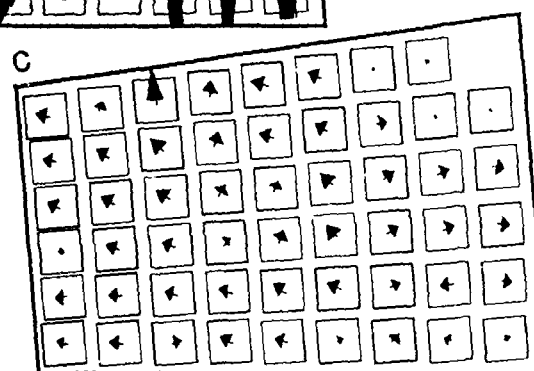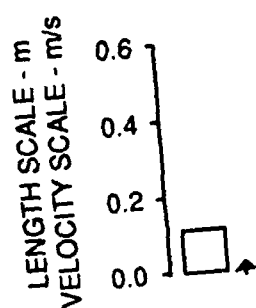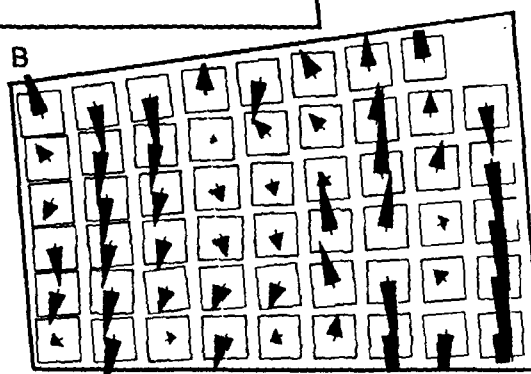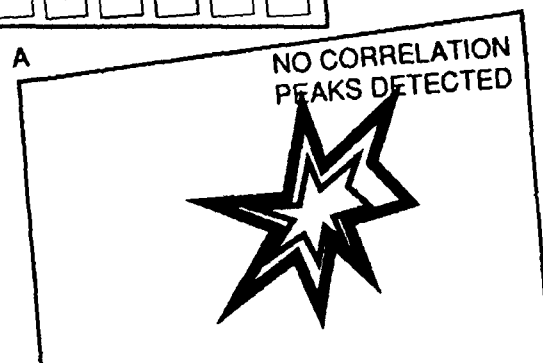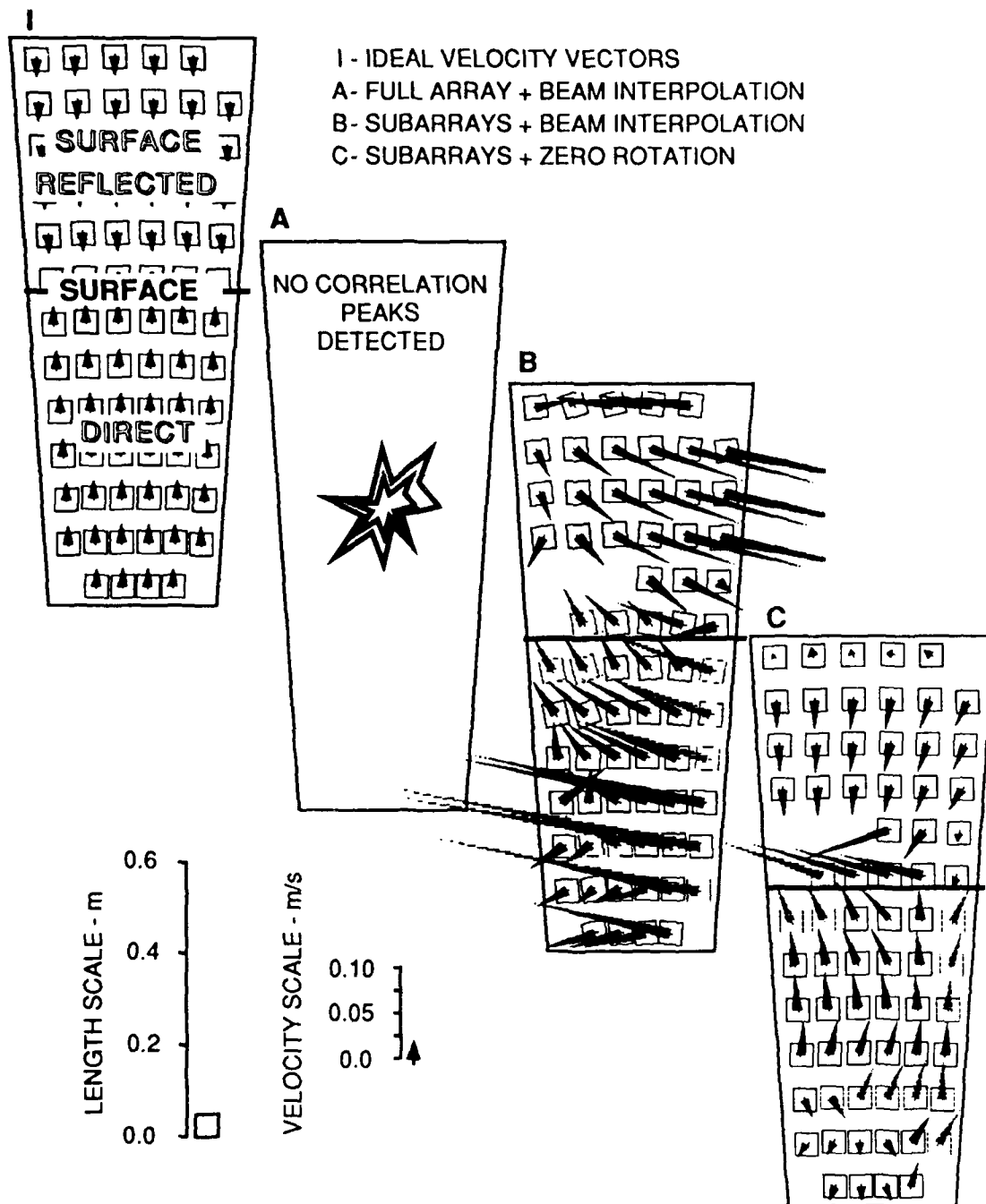**FIGURE 7.10**
RESULTS FROM BUBBLE STREAM IN THE AXIAL DIRECTION

63

7.3.2 Field Experiments

The results obtained by computer simulation and by the tank experiments indicated that, under certain conditions, Method C can be expected to give reasonable estimates of the flow field. According to the project plan, the sonar system was taken to Lake Travis Test Station (LTTS) for further tests. Unfortunately, the conditions at LTTS were extremely calm without any prospect for change in the near term. Consequently, there were no scatterers in the water that the sonar could detect.

To obtain a more cooperative environment, a coastal site was selected instead. The site chosen was Port Aransas. The director and staff of The University of Texas Marine Science Center at Port Aransas were very cooperative, allowing us to use their pier laboratory, which is a laboratory with work benches and power supplies constructed on a pier that extends into a ship channel (shown in Fig. 7.11). The currents in the ship channel were driven by tidal forces. The water depth at the end of the pier was 6 m (20 ft). Initially, the conditions there were also extremely calm, but on the second day of our visit, the winds picked up and it rained heavily. We were able to detect considerable volume and surface backscatter for motion processing.

The transducers were deployed using a portable column. A photograph of the assembly resting on the lower deck of the pier is shown in Fig. 7.12. When deployed, the back of the transducers was wedged to a support structure such as a piling; the force of the tidal current in conjunction with a back plate with a serrated notch kept the transducers firmly wedged in place until the tide turned, as shown in Fig. 7.13. A plan view of the sonar deployment for incoming and outgoing tides is shown in Fig. 7.14. Unfortunately, it was not possible with the fittings that we had to fasten the transducers to any of the external pilings. Therefore, the flow reaching the transducers was obstructed to some extent.

An example of the results obtained of volume motion on the incoming tide is shown in Fig. 7.15. In this case, the surface is outside and above the field of view. It is seen that Method A was unable to produce any correlation peaks. Method B gave velocity estimates that were too large and too spurious to be credible.

FIGURE 7.11
PHOTOGRAPH OF THE PIER LABORATORY AT PORT ARANSAS

5706-2

FIGURE 7.12
PHOTOGRAPH OF THE TRANSDUCER ASSEMBLY
ATTACHED TO THE PORTABLE COLUMN RESTING ON THE LOWER DECK OF THE PIER
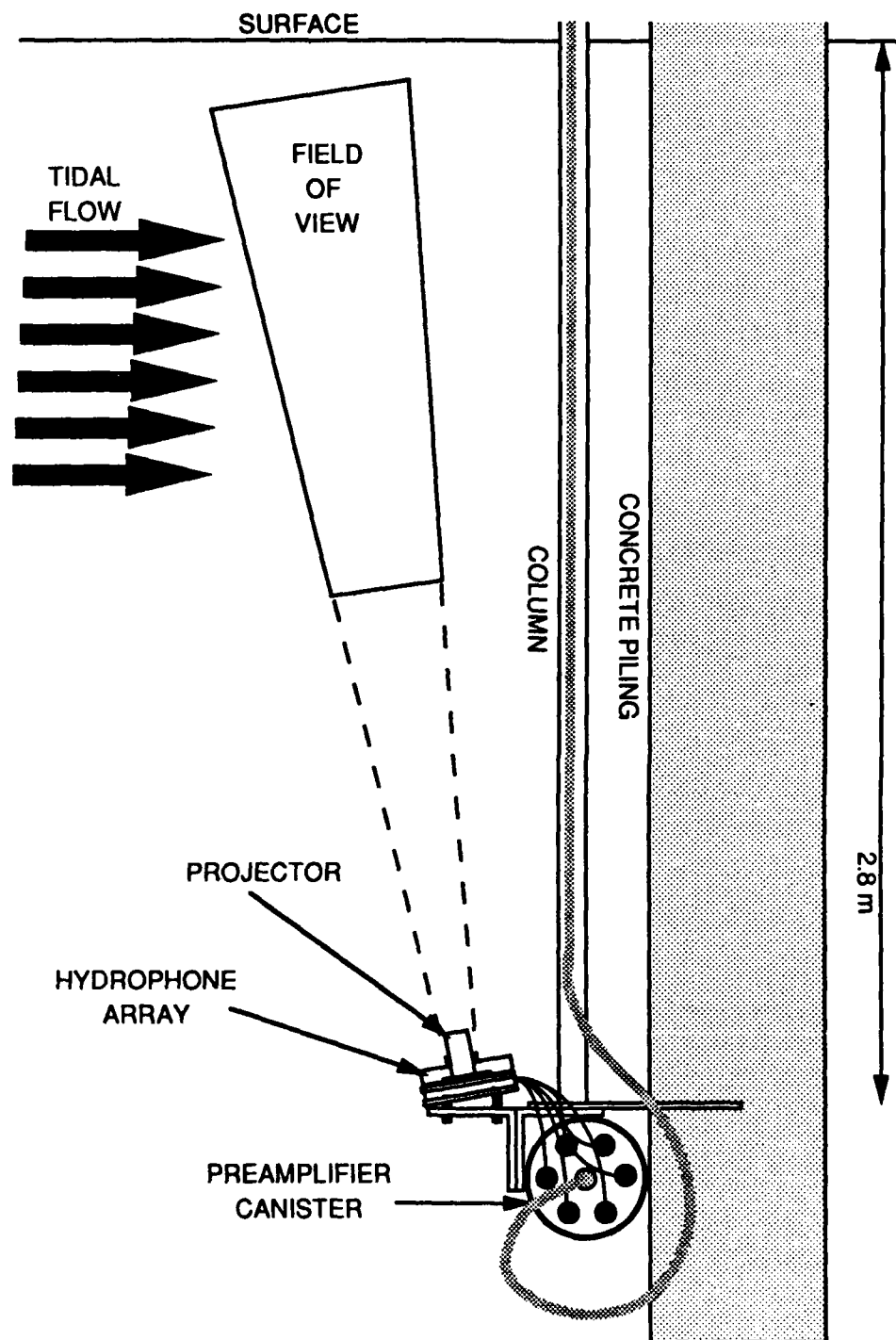
66

FIGURE 7.13
DEPLOYMENT OF REMOTE SENSING SONAR AT PORT ARANSAS:
ELEVATION

67
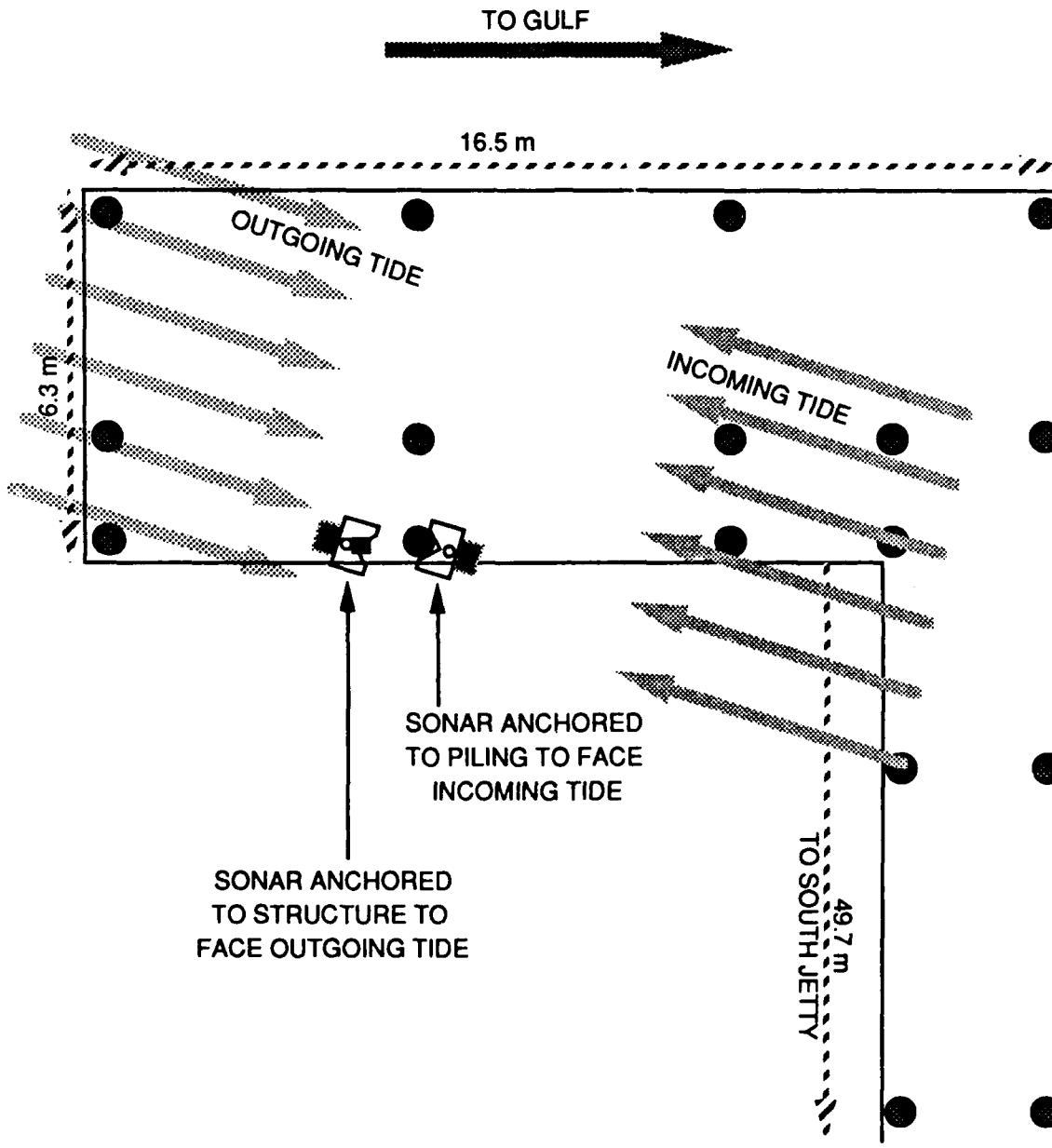
FIGURE 7.14
DEPLOYMENT OF REMOTE SENSING SONAR AT PORT ARANSAS:
PLAN VIEW

I - IDEAL VELOCITY VECTORS
A - FULL ARRAY + BEAM INTERPOLATION
B - SUBARRAYS + BEAM INTERPOLATION
C - SUBARRAYS + ZERO ROTATION

FIGURE 7.15
EXAMPLE OF RESULTS ON INCOMING TIDE, PORT ARANSAS

69

Method C gave results that appeared to be not unreasonable, and indicative of strong turbulent activity. As with the bubble experiments in the tank, there was no way of checking the precise validity of the results. The situation is also complicated by the presence of fish. However, from our computer simulation studies we know that Method C is liable to give erroneous azimuthal motion estimates if there is significant rotational motion present. Therefore, where the results show little or no azimuthal motion, they are unlikely to be erroneous. The results indicate significantly greater activity in the upper half of the field of view, with regions of large vertical components of motion, probably associated with surface wave activity. Comparable horizontal components of motion must also be present but were not detectable because the waves were moving perpendicularly to the plane of the field of view (y direction). We had chosen to align the field of view with the tidal current, and unfortunately the tidal current and the waves were moving in orthogonal directions. This is an unavoidable problem of a two-dimensional sensing system in a three-dimensional environment. The less active region in the lower part of the field of view is probably more closely connected with the tidal current. The blank regions are where correlation peaks were not detected, indicative of either strong rotational motion or flow perpendicular to the plane of the field of view. The results from a sequence of pings produced by Method C are shown in Fig. 7.16. It is seen that, occasionally, large azimuthal movements are indicated; they should be interpreted as rotational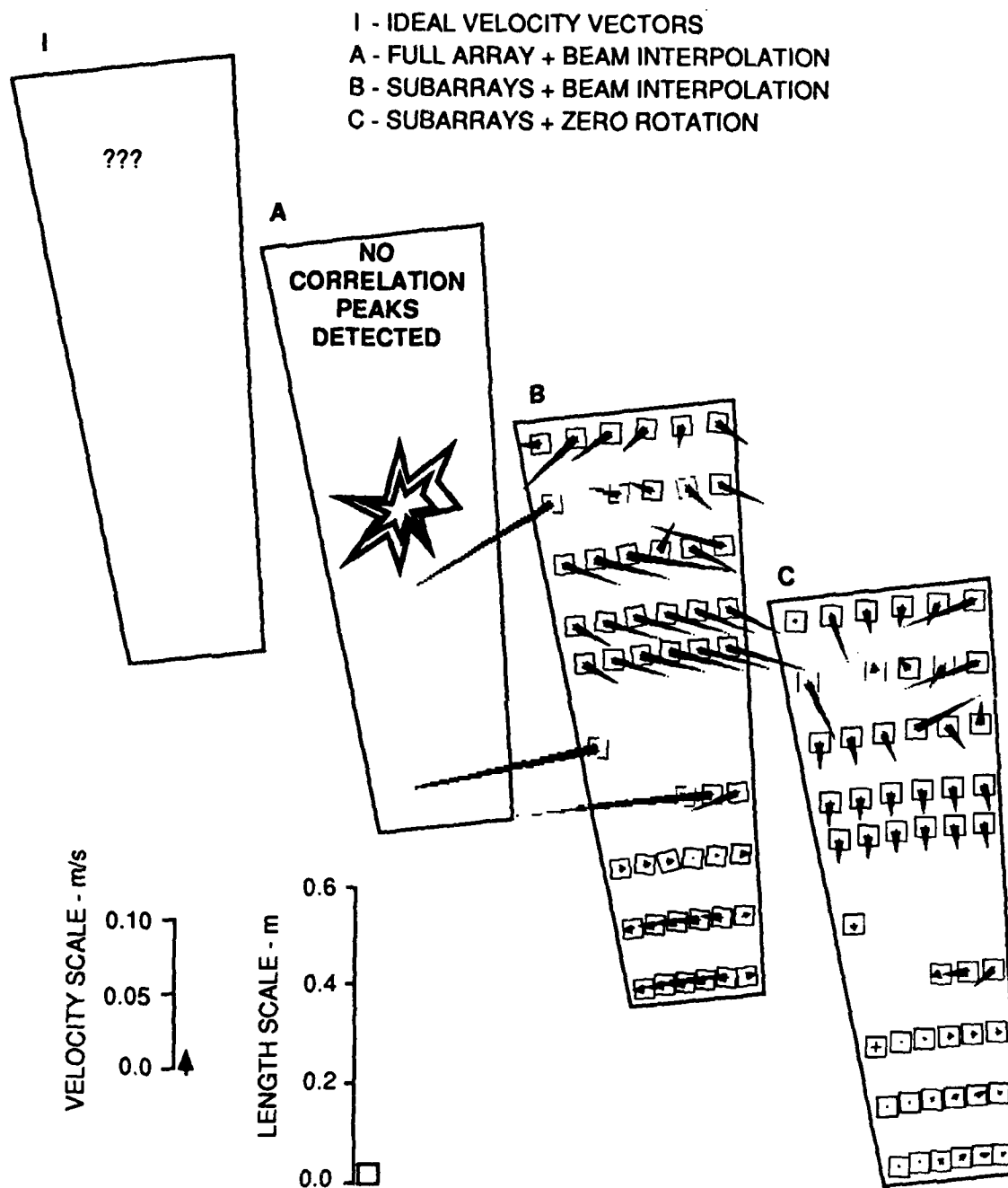 motion such as eddies. It is seen that the velocities in the upper part of the field of view have completely changed direction over this short sequence. The large azimuthal velocities indicated near the middle are probably indicative of strong rotational or shearing motion. The region near the bottom shows relatively little activity.

Data showing the surface backscatter were taken as the wake from a passing vessel passed over the instruments. It was raining at the time, giving the water surface a small scale roughness. For observing the surface, the whole array is used to form a fan of 12 overlapping beams. The geometry is shown in Fig. 7.17. It is clear that the geometry is far from ideal because the wave was traveling in the y direction, orthogonal to the orientation of the transducers. An example of the results is shown in Fig. 7.18. The plotted points correspond to the range and angle of the detected backscattered peaks. In Fig. 7.18(a), every tenth ping from a
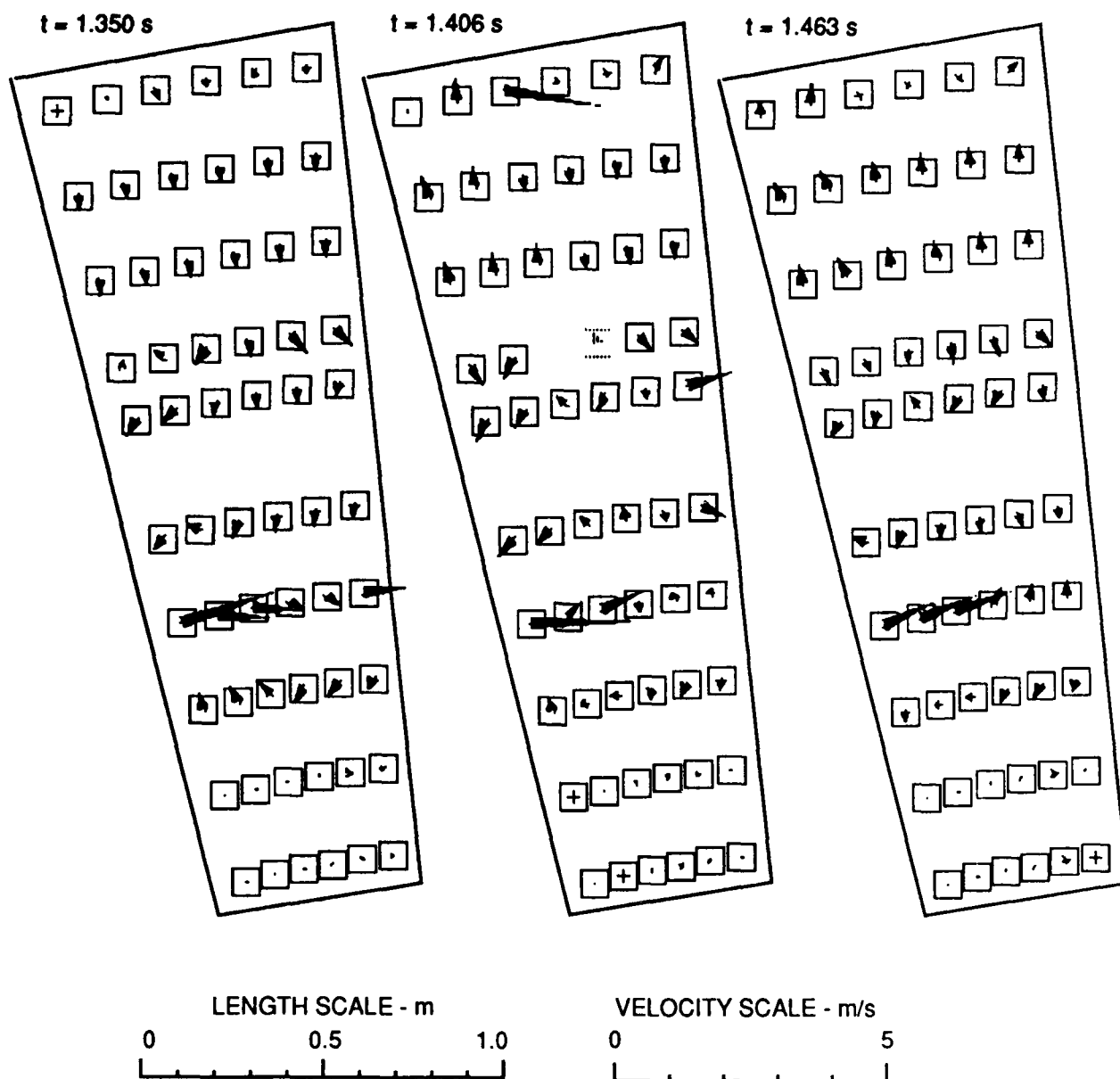
FIGURE 7.16
EXAMPLE OF THREE-PING SEQUENCE OF VOLUME MOTION
USING METHOD C

71
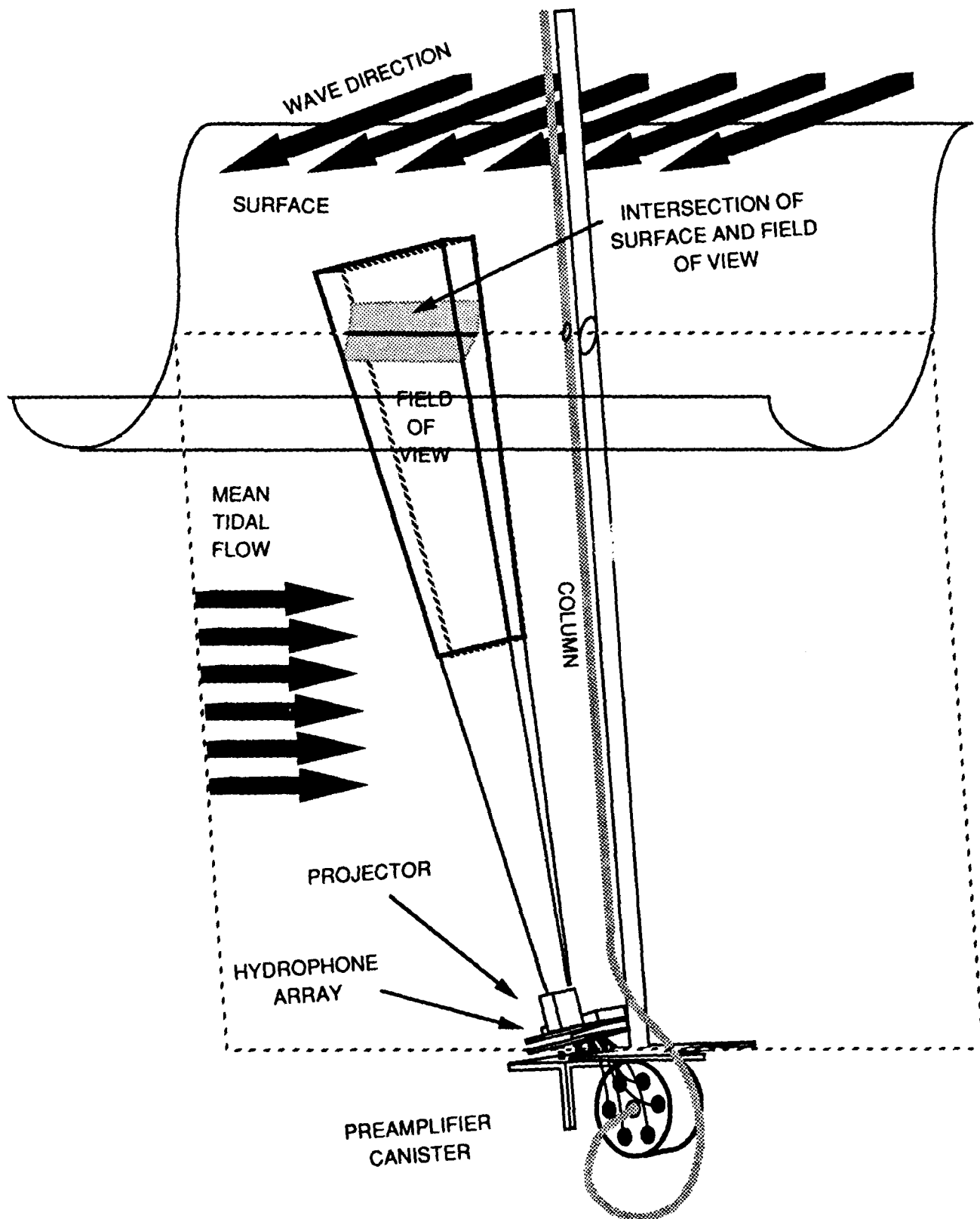
FIGURE 7.17
GEOMETRY OF SURFACE WAVE SENSING ON OUTGOING TIDE

SCALE - m

0   0.5   1.0

PING 40   PING 50   PING 60   PING 70   PING 80

t = 1.706 s   t = 2.144 s   t = 2.581 s   t = 3.019 s   t = 3.456 s
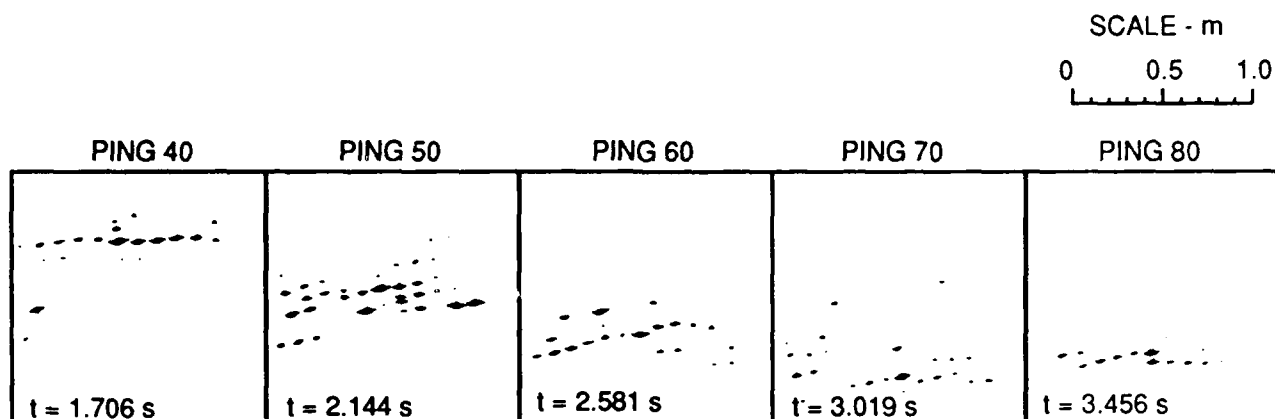
(a)
EVERY TENTH PING FROM A
SERIES OF 50

SCALE - m

0   0.5   1.0

PING 85   PING 86   PING 87   PING 88

t = 3.675 s   t = 3.719 s   t = 3.763 s   t = 3.806 s
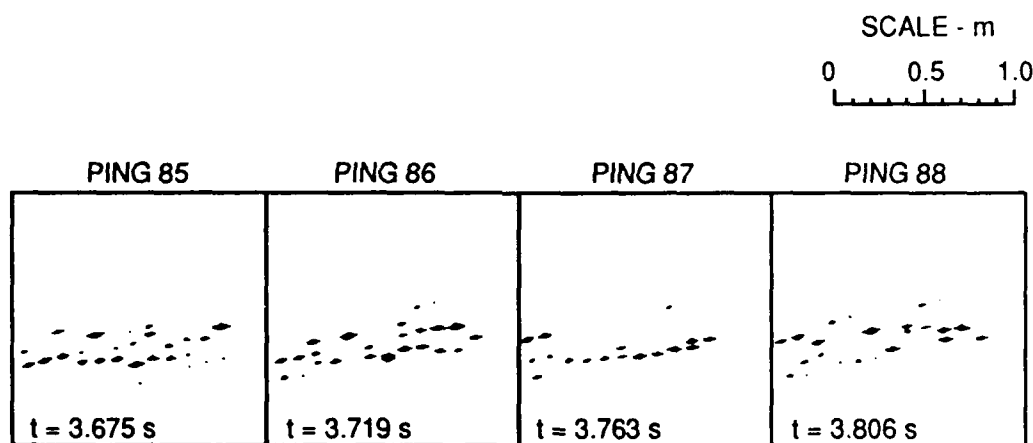
(b)
A SEQUENCE OF FOUR
CONSECUTIVE PINGS

FIGURE 7.18
EXAMPLES OF BACKSCATTER FROM THE SURFACE

sequence of 50 pings is shown. The ping period was 40 ms. The downward motion of a wave is captured in this sequence. It is seen that, most of the time, the surface profile is not well defined. A sequence of four consecutive pings is shown in Fig. 7.18(b); these appear to show the surface backscatter consisting of random components superimposed on a relatively stable profile. Part of the problem may be due to beam-beam crosstalk through the sidelobes and multiple reflections. A major contributing cause is the direction of wave propagation, which was orthogonal to the fan of formed beams.

The volume velocity results obtained by Method C for the first three pings shown in Fig. 7.18(a) are superimposed on the surface profiles in Fig. 7.19. It is seen that in the vicinity of the surface, very few crosscorrelation peaks are detected. In the first ping, near the middle of the field of view, there is a region of relative calm where the water is momentarily at rest. Moving farther down, there is a region in which crosscorrelations are not detectable, probably due to currents moving orthogonally to the plane of the field of view--a consequence of the two-dimensional limitation. At the bottom of the field there is a region where the water is moving downward. In the second and third pings, it is seen that the velocity in this region has changed direction.

In spite of the gaps, the foregoing examples illustrate the physical insights that an acoustic remote sensing sonar can provide.

FIGURE 7.19
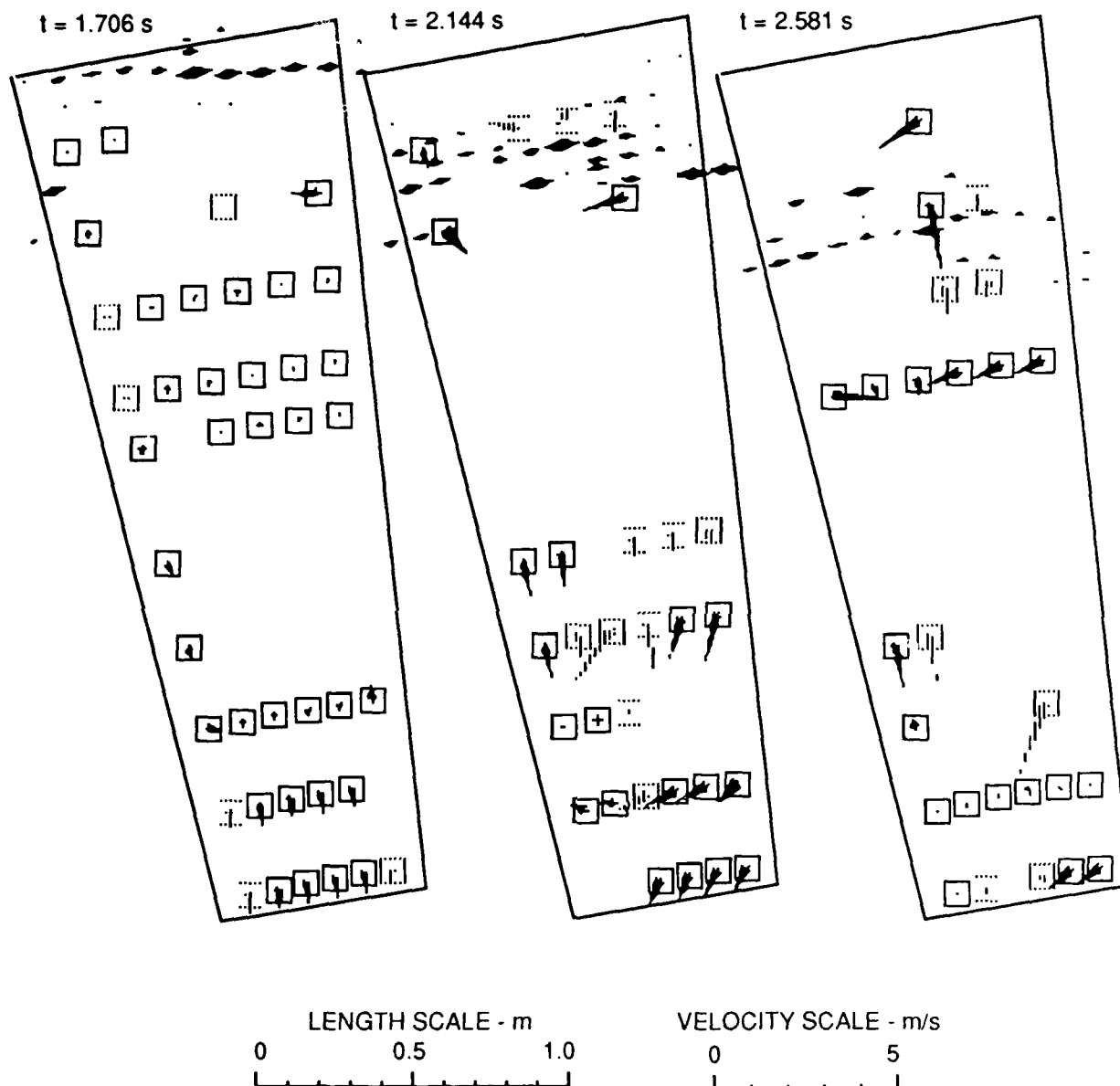**EXAMPLE OF THREE-PING SEQUENCE OF SURFACE AND VOLUME MOTION**
USING METHOD C

8. CONCLUSIONS AND PLANS

8.1 CONCLUSIONS

Acoustic remote sensing of ocean surface and volume movements is possible if two main requirements can be met. The first requirement is directed at the environment. That is, there must be sufficient acoustic backscattering strength. In the case of surface remote sensing, the surface must have a minimum level of roughness, such as wind generated capillary waves or rain generated ripples. In the case of volume remote sensing, there must be sufficient volume backscatter from passive riders, such as plankton or bubbles. The second requirement is directed at the equipment. That is, there must be an array of sufficient size, a signal of sufficient bandwidth and, most important, a processing algorithm that can interpret surface and volume motion from the backscatter.

With regard to the environmental requirement, our experimental results at Port Aransas on the Gulf Coast demonstrate that the environmental conditions can be satisfied. We were able to detect backscatter from the water surface and volume in rainy conditions. Further tests are required over a wide range of sea states to establish minimum criteria for surface and volume remote sensing.

With regard to the equipment requirement, we have built a small line array with the necessary bandwidth and source level to carry out a limited demonstration of acoustic remote sensing. The most difficult part was the development of the processing algorithm.

Our approach was to track volume movement by the acoustic backscatter signature of each resolution cell through the crosscorrelation function of the backscatter from ping to ping. Three algorithms were developed to track volume motion: Methods A, B, and C. All three used the ping-to-ping delay shift of the crosscorrelation function to estimate the radial component of motion, otherwise known as the pulse-to-pulse Doppler method. They differ in the methods for estimating azimuthal motion and in the degree of wavefront coherence assumed. Method A assumes coherent wavefronts and employs the full hydrophone array to form a set of beams, and tracks azimuthal motion by beam interpolation. Methods B and C use subsets of the hydrophone array, called subarrays, to form

77

several sets of beams. Method B implicitly assumes that coherent wavefronts exist over the subarray. In Method B, the migration of the acoustic signature is tracked both across the subarrays and across the beams; beam interpolation is used to determine angle of arrival. Estimates of azimuthal motion and rotation of the volume are produced. In Method C, the migration of the acoustic signature is tracked across the subarrays but no attempt is made to determine the angle of arrival; a zero rotation assumption is necessary to estimate azimuthal motion. Method C only uses beamforming to partition the field of view into resolution cells, but otherwise makes no assumptions regarding the existence of a wavefront.

Methods A and B were found to perform poorly. Method C was successfully demonstrated for translational motion using computer simulated data, and in laboratory experiments with both a moving wall and a bubble stream. Field experiments gave credible results but were difficult to judge due to the lack of an independent standard.

The failure of Methods A and B indicates that the acoustic backscatter signature should more appropriately be considered as a speckle pattern that changes with both range and angle. The combined effects of azimuthal motion and rotation of the scattering volume causes the speckle pattern to migrate across the hydrophone array. The migration of the pattern is a measurable effect, as successfully demonstrated by the multi-subarray approach used in Methods B and C.

Acoustic profiling of surface waves was demonstrated using the wake of a passing ship. The results in this study were obtained with a surface roughened by rain. The quality of the results was rather poor due to a lack of alignment between wave direction and the acoustic beams, and due to interference effects, possibly due to beam-beam crosstalk through sidelobes and multiple surface reflections. These problems arise because of the highly reflective nature of the surface. Specular returns are very strong in relation to backscatter from other angles of incidence causing crosstalk between adjacent beams through the sidelobes. The orientation of surface facets may occasionally produce corner reflector-like structures causing multiple reflections. These problems may be reduced by careful array design for minimal sidelobes. They are also reduced as the surface

roughness increases. Thus, acoustic profiling of the ocean surface at sea state numbers above a certain minimum level may be quite successful.

8.2 BENEFITS

Although we have not yet achieved a comprehensive remote sensing algorithm, the multi-subarray approach appears to be a step in the right direction. It has a couple of properties that can be immediately applied to benefit related applications.

The multi-subarray approach can discriminate between discrete and distributed scatterers. Discrimination is possible because the backscatter from a discrete scatterer has a coherent wavefront while that of a distributed cloud of scatterers does not. This difference is not detectable with beamformed arrays where the whole array is used to form the beam and the existence of a wavefront is implicitly assumed. With the multi-subarray, the difference is detectable in the form of backscatter coherence, or lack of it, between the subarrays.

The multi-subarray approach can also recover radial crosscorrelation signals which normally would be lost due to rotation or shear deformation of the scatterer cloud. This was demonstrated in the last five computer simulated test cases, and in the experiments both in the tank and in the field. In these cases, it was found that beamforming using the total array was unable to recover the backscatter signature from one ping to the next, making it impossible to reliably perform pulse-to-pulse Doppler processing. In practice, this problem may be overcome to some ex ant by averaging for long periods, because it is likely that there will be a few short intervals within the averaging window in which the deformation rate goes through zeroes and correlation is briefly achieved. As demonstrated in the test cases, the multi-subarray approach can track the acoustic signature and produce accurate radial Doppler estimates, where a regular beamformer cannot, and without lengthy averaging. This property may be used to improve the performance of existing pulse-to-pulse Doppler sonars.

8.3 PLANS

Building on the above results, we plan to develop a comprehensive algorithm for estimating azimuthal motion, including translation and rotation, that does not rely on coherent wavefronts. We have found one component of this algorithm, that is, the multi-subarray method, which detects the migration of the backscattered speckle pattern. The migration, however, is not caused by azimuthal translation alone, but by a combination of rotational and translational motion. In an irrotational fluid this method will directly give accurate estimates of azimuthal motion. In a rotational fluid, another independent estimator is required to unravel the rotational and translational components. One approach is to obtain an independent estimate of volume rotation. This may be done by using the angular gradient of the radial component of motion. Another approach is to obtain an independent measure of azimuthal motion; a partial solution may be found in the vector gradient of the radial velocity, which may be used to estimate the relative changes in azimuthal motion by the divergence theorem.

With regard to surface motion, an analysis will be made regarding the sidelobe levels and sea state numbers necessary for successful surface profiling. A linking algorithm will also be implemented to link the acoustic peaks into a continuous surface function. The algorithm will be applicable to both surfaces and interfaces such as plankton layers.

The above studies will be carried out mainly by computer simulations based on the simulation model developed here which has been successfully used to identify the problems in the initial approach and to develop and test a number of algorithms. The simulations will not be limited to any small experimental system, but will be extended to a full scale system for three-dimensional motion sensing. The expected results will include design parameters such as array sizes, signal bandwidths and processing complexity, and performance predictions including motion estimation accuracies under a variety of conditions and performance limitations, with supporting animated sequences.

REFERENCES

1. N. P. Chotiros, "Design Study of Remote Sensing for Ocean Surface and Interior Activity," Applied Research Laboratories Technical Report No. 86-38 (ARL-TR-86-38), Applied Research Laboratories, The University of Texas at Austin, 31 December 1986.

2. J. Christensen Cutchin, R. Knoop, J. Stillman, and W. Woodward, "Acoustic Doppler Current Profiling from a Volunteer Commercial Ship," Proceedings of IEEE Third Working Conference on Current Measurement, CH2305-1/86/0000-0098, January 1986.

3. W. E. Woodward and G. F. Appell, "Current Velocity Measurements Using Acoustic Doppler Backscatter: A Review," IEEE J. Oceanic Eng. QE-11, No. 1, 3-6 (1986).

4. R. Pinkel, "The Use of Acoustic Doppler Sonar for Upper Ocean Velocity Measurements," MPL-U-86/07, Marine Physical Laboratory of the Scripps Institution of Oceanography, The University of California, San Diego, California, 1986.

5. R. Lehrmitte and R. Serafin, "Pulse-to-Pulse Coherent Doppler Sonar Signal Processing," J. Atmos. Oceanic Technol. 1, No. 4 (1984).

6. S. F. Clifford and D. M. Farmer, "Space-Time Analysis of Acoustic Scintillations in Ocean Current Sensing," Proceedings of IEEE Third Working Conference on Current Measurement, CH2305-1,78-81, January 1986.

7. J. Coultard, "Ultrasonic Cross-Correlation Flowmeters," Ultrasonics 11, No. 2, 83-88 (1973), also British Patents 32563/70 and 2593/71.

8. F. R. Dickey, Jr., and J. A. Edward, "Velocity Measurement Using Correlation Sonar," (EHM-12, 730) IEEE PLANS 1978, Position Location and Navigation Symposium, San Diego, California, 6-9 November 1978.

9.   P. Atkins and B. V. Smith, "The Predicted Performance of an Underwater Navigation System Based on a Correlation Log," Proceedings of the Institute of Acoustics, Vol. 9, Part 4, Underwater Communication and Position Fixing Conference, 17-18 December 1987.

10.   N. P. Chotiros, Progress Summary under Contract N00014-87-K-0392, 10 May 1988.

DISTRIBUTION LIST FOR
ARL-TR-89-4
UNDER CONTRACT N00014-87-K-0392

Copy No.

Office of the Chief of Naval Research
Department of the Navy
Arlington, VA 22217-5000
1   Attn: R. Obrochta (Code 1125AR)
2   N. Huang (Code 1120PO)
3   T. Curtin (Code 1125AR)
4   F. Fitzgerald (Code1125AO)
5   T. Spence (Code 1122PO)
6   M. Orr (Code 1125AO)

Director
Naval Research Laboratory
Washington, DC 20375
7 - 12   Attn: Code 2627

Director
Woods Hole Oceanographic Institution
Smith 2
Woods Hole, MA 02543
13   Attn: G. Terray
14   B. Brumley

The University of Miami
Rosensteil School of Marine and Atmospheric Science
Division of Morphology and Physical Oceanography
Miami, FL 33149
15   Attn: R. Lhermitte

Commanding Officer
Naval Ocean Research and Development Activity
Stennis Space Center, MS 39529-5004
16   Attn: R. Farwell
17   T. Goldsberry

Commanding Officer
Naval Ocean Systems Center
San Diego, CA 92152
18   Attn: K. Richter (Code 522)
19   R. McLennan (Code 19)
20   R. Anderson (Code 19)

Copy No.

	Director
	Department of the Army
	Waterways Experiment Station, Corps of Engineers
	P.O. Box 631
	Vicksburg, MS 39180-0631
21	Attn: T. E. White

Commanding Officer and Director
Defense Technical Information Center
Bldg. 5, Cameron Station
5010 Duke St.
22 - 33   Alexandria, VA 22314

Tracor, Inc.
3420 Kenyon Street
Suite 209
San Diego, CA 92110
34   Attn: D. V. Holliday

Director
Marine Physical Laboratory
Scripps Institution of Oceanography
University of California at San Diego
La Jolla, CA 92106
35   Attn: R. Pinkel

The University of Texas at Austin
Marine Science Center
Port Aransas, TX 78373-1267
36   Attn: Dr. J. Thompson
37   Dr. A. Amos

38   Dr. J. K. Lewis
Science Applications International Corporation
1304 Deacon
College Station, TX 77840

39   Garland R. Barnard, ARL:UT

40   Hollis Boehme, ARL:UT

41   Nicholas P. Chotiros, ARL:UT

42   Harlan G. Frey, ARL:UT

43   John M. Huckabay, ARL:UT

44   Charles M. Loeffler, ARL:UT

Distribution List for ARL-TR-89-4 under Contract N00014-87-K-0392
(cont'd)

<u>Copy No.</u>

45   Library, ARL:UT

46 - 51   Reserve, ARL:UT